

SEARCH FOR GEV GAMMA RAY BURSTS WITH THE ARGO-YBJ DETECTOR: SUMMARY OF EIGHT YEARS OF OBSERVATIONS

B. Bartoli^{1,2}, P. Bernardini^{3,4}, X.J. Bi⁵, P. Branchini⁶, A. Budano⁶, P. Camarri^{7,8}, Z. Cao⁵,
 R. Cardarelli⁸, S. Catalanotti^{1,2}, S.Z. Chen⁵, T.L. Chen⁹, P. Creti⁴, S.W. Cui¹⁰, B.Z. Dai¹¹,
 A. D'Amone^{3,4}, Danzengluobu⁹, I. De Mitri^{3,4}, B. D'Ettorre Piazzoli^{1,2}, T. Di Girolamo^{1,2,*},
 G. Di Sciascio⁸, C.F. Feng¹², Zhaoyang Feng⁵, Zhenyong Feng¹³, Q.B. Gou⁵, Y.Q. Guo⁵,
 H.H. He⁵, Haibing Hu⁹, Hongbo Hu⁵, M. Iacovacci^{1,2}, R. Iuppa^{7,8}, H.Y. Jia¹³, Labaciren⁹,
 H.J. Li⁹, G. Liguori^{14,15}, C. Liu⁵, J. Liu¹¹, M.Y. Liu⁹, H. Lu⁵, L.L. Ma⁵, X.H. Ma⁵,
 G. Mancarella^{3,4}, S.M. Mari^{6,16}, G. Marsella^{3,4}, D. Martello^{3,4}, S. Mastroianni²,
 P. Montini^{6,16}, C.C. Ning⁹, M. Panareo^{3,4}, L. Perrone^{3,4}, P. Pistilli^{6,16}, F. Ruggieri⁶,
 P. Salvini¹⁵, R. Santonico^{7,8}, P.R. Shen⁵, X.D. Sheng⁵, F. Shi⁵, A. Surdo⁴, Y.H. Tan⁵,
 P. Vallania^{17,18,*}, S. Vernetto^{17,18}, C. Vigorito^{18,19,*}, H. Wang⁵, C.Y. Wu⁵, H.R. Wu⁵,
 L. Xue¹², Q.Y. Yang¹¹, X.C. Yang¹¹, Z.G. Yao⁵, A.F. Yuan⁹, M. Zha⁵, H.M. Zhang⁵,
 L. Zhang¹¹, X.Y. Zhang¹², Y. Zhang⁵, J. Zhao⁵, Zhaxiciren⁹, Zhaxisangzhu⁹, X.X. Zhou¹³,
 F.R. Zhu¹³, Q.Q. Zhu⁵ and G. Zizzi²⁰

(The ARGO-YBJ Collaboration)

*Corresponding authors: digirola@na.infn.it, Piero.Vallania@to.infn.it, vig-orito@to.infn.it

¹Dipartimento di Fisica dell’Università di Napoli “Federico II”, Complesso Universitario di Monte Sant’Angelo, via Cinthia, 80126 Napoli, Italy.

²Istituto Nazionale di Fisica Nucleare, Sezione di Napoli, Complesso Universitario di Monte Sant’Angelo, via Cinthia, 80126 Napoli, Italy.

³Dipartimento Matematica e Fisica “Ennio De Giorgi”, Università del Salento, via per Arnesano, 73100 Lecce, Italy.

⁴Istituto Nazionale di Fisica Nucleare, Sezione di Lecce, via per Arnesano, 73100 Lecce, Italy.

⁵Key Laboratory of Particle Astrophysics, Institute of High Energy Physics, Chinese Academy of Sciences, P.O. Box 918, 100049 Beijing, P.R. China.

⁶Istituto Nazionale di Fisica Nucleare, Sezione di Roma Tre, via della Vasca Navale 84, 00146 Roma, Italy.

⁷Dipartimento di Fisica dell’Università di Roma “Tor Vergata”, via della Ricerca Scientifica 1, 00133 Roma, Italy.

⁸Istituto Nazionale di Fisica Nucleare, Sezione di Roma Tor Vergata, via della Ricerca Scientifica 1, 00133 Roma, Italy.

⁹Tibet University, 850000 Lhasa, Xizang, P.R. China.

¹⁰Hebei Normal University, Shijiazhuang 050016, Hebei, P.R. China.

¹¹Yunnan University, 2 North Cuihu Rd., 650091 Kunming, Yunnan, P.R. China.

¹²Shandong University, 250100 Jinan, Shandong, P.R. China.

¹³Southwest Jiaotong University, 610031 Chengdu, Sichuan, P.R. China.

¹⁴Dipartimento di Fisica dell’Università di Pavia, via Bassi 6, 27100 Pavia, Italy.

¹⁵Istituto Nazionale di Fisica Nucleare, Sezione di Pavia, via Bassi 6, 27100 Pavia, Italy.

¹⁶Dipartimento di Fisica dell’Università “Roma Tre”, via della Vasca Navale 84, 00146

Received _____; accepted _____

Roma, Italy.

¹⁷Osservatorio Astrofisico di Torino dell'Istituto Nazionale di Astrofisica, via P. Giuria 1, 10125 Torino, Italy.

¹⁸Istituto Nazionale di Fisica Nucleare, Sezione di Torino, via P. Giuria 1, 10125 Torino, Italy.

¹⁹Dipartimento di Fisica dell'Università di Torino, via P. Giuria 1, 10125 Torino, Italy.

²⁰Istituto Nazionale di Fisica Nucleare - CNAF, Viale Berti-Pichat 6/2, 40127 Bologna, Italy.

ABSTRACT

The search for Gamma Ray Burst (GRB) emission in the energy range 1-100 GeV in coincidence with the satellite detection has been carried out using the Astrophysical Radiation with Ground-based Observatory at YangBaJing (ARGO-YBJ) experiment. The high altitude location (4300 m a.s.l.), the large active surface ($\sim 6700 \text{ m}^2$ of Resistive Plate Chambers), the wide field of view ($\sim 2 \text{ sr}$, limited only by the atmospheric absorption) and the high duty cycle ($> 86 \%$) make the ARGO-YBJ experiment particularly suitable to detect short and unexpected events like GRBs. With the scaler mode technique, i.e., counting all the particles hitting the detector with no measurement of the primary energy and arrival direction, the minimum threshold of $\sim 1 \text{ GeV}$ can be reached, overlapping the direct measurements carried out by satellites. During the experiment lifetime, from December 17, 2004 to February 7, 2013, a total of 206 GRBs occurring within the ARGO-YBJ field of view (zenith angle $\theta \leq 45^\circ$) have been analyzed. This is the largest sample of GRBs investigated with a ground-based detector. Two lightcurve models have been assumed and since in both cases no significant excess has been found, the corresponding fluence upper limits in the 1-100 GeV energy region have been derived, with values as low as $10^{-5} \text{ erg cm}^{-2}$. The analysis of a subset of 24 GRBs with known redshift has been used to constrain the fluence extrapolation to the GeV region together with possible cutoffs under different assumptions on the spectrum.

Subject headings: gamma rays: bursts — gamma rays: observations

1. INTRODUCTION

Gamma Ray Bursts (GRBs) are among the most powerful sources in the sky, covering a very wide energy range from radio to multi-GeV γ -rays. Even though they are located at cosmological distances (Costa et al. 1997) at higher energies they outshine all other sources, including the Sun, during their typical duration of a few seconds. GRBs occur at an average rate of a few per day, coming from the whole Universe. Their high energy spectrum shows different features, the most important being a peak in the keV-MeV region. There are at least two classes of GRBs, classified in terms of burst duration. Short GRBs last up to 2 s and show a harder spectrum with a typical peak energy in the νF_ν spectrum at Earth at ~ 490 keV (Nava et al. 2011). Their origin is believed to be due to the merging of two compact objects like neutron stars or a neutron star and a black hole (Ruffert & Janka 1999; Rosswog et al. 2003). Recent support for this model comes from the optical and near-infrared detection of a faint transient, known as “kilonova”, in the days following the short GRB130603B (Tanvir et al. 2013). Long GRBs have duration greater than 2 s with a softer spectrum and a typical νF_ν peak around 160 keV (Nava et al. 2011). In this case the origin is believed to be due to the core collapse of type Ic supernovae, and indeed the coincidence of the two events has been observed in several cases (see for example Weiler et al. (2001); Stanek et al. (2003); Gal-Yam et al. (2004); Campana et al. (2006)). Most of the GRB spectra can be described by the Band function (Band et al. 1993), composed of two smoothly joined power laws. This function fits quite successfully the convex shape and broad peak of the spectral energy distribution of the GRB prompt emission, however, being a phenomenological model, it does not take into account any physical explanation concerning either the acceleration processes or non-thermal radiative losses. Despite the bulk emission is concentrated in the keV-MeV energy region, EGRET (Kanbach et al. 1988) and more recently Fermi (Meegan et al. 2009) and AGILE (Longo et al. 2012) satellites observed photons in the MeV-GeV range.

At the time of writing this paper, the highest photon energy measured at Earth is 95 GeV, observed by the LAT instrument on the Fermi satellite from GRB130427A (Ackermann et al. 2014). The highest intrinsic energy (~ 147 GeV) detected from a GRB comes from a 27.4 GeV γ -ray observed during GRB080916C, which has a redshift of 4.35. This γ -ray was previously missed by the Fermi-LAT event analysis and was recently recovered using an improved data analysis (Atwood et al. 2013). Previously, the maximum observed photon energy was 33.4 GeV from GRB090902B (~ 94 GeV when corrected for its redshift $z=1.822$). Up to now (May 2014) after almost 6 years of operation, Fermi-LAT detected photons above 10 GeV from one short (GRB090510) and 8 long GRBs (Abdo et al. 2009a,b; Ackermann et al. 2010, 2011, 2013, 2014; Kocevski et al. 2013; Vianello et al. 2013). Some of these GRBs (namely, GRB08916C, GRB090510, GRB090902B, GRB090926A, GRB130427A) cannot be well described at GeV energies with an extrapolation of the Band function seen at keV-MeV energies, but require a much harder energy spectrum starting from ~ 100 MeV with a photon index $\alpha \sim -2$.

Another feature which characterizes the GeV emission is the light curve, with its onset delayed with respect to the keV-MeV range and a longer duration, appearing as a very high energy afterglow. The current models include emission in both internal (Guetta & Granot 2003; Finke et al. 2008) and external (Kumar & Barniol Duran 2010; Ghisellini et al. 2010; Ghirlanda et al. 2010) shock scenarios, with γ -rays produced by leptonic or hadronic processes via inverse Compton scattering or neutral pion decay. The emission is believed to happen in highly relativistic narrow jets pointing towards the Earth. The study of the GeV energy region could be of great help in discriminating between different models. As an example, the delayed onset of the high energy emission seen in most LAT-detected GRBs, if intrinsic, should favour the production from external shocks in the early GRB afterglow (Fan et al. 2008) instead of the reverse shock formed when the GRB ejecta encounter the interstellar medium (Wang et al. 2005).

GRBs have been detected through the whole universe, from the local one to redshift $z=8.2$, corresponding to $\sim 95\%$ of the age of the universe. Unfortunately, the energy resolution of the instruments onboard Fermi prevents the detection of clear spectral lines while their large angular uncertainty hampers the optical identification and follow-up. For these reasons, only the GRBs seen in the keV-MeV region with arcmin resolution (as with Swift-BAT) have a measured redshift. In this same energy region the spectral index is usually measured but when the detected signal is weak also the time-averaged spectrum is poorly constrained. The absorption in the Extragalactic Background Light (EBL) greatly reduces the high energy photon flux from extragalactic sources. The detection of > 10 GeV photons from high redshift sources can be used to constrain the EBL amount from regions where it is highly uncertain. Finally, the spectral slope in the GeV region could be of great help in discriminating between different GRB models. In particular, the detection of a cutoff energy could be indicative of e-pair production at source allowing the measurement of the Lorentz boost factor of the jet (Ackermann et al. 2011). On the other hand, the spectral cutoff may be due to attenuation by the EBL, thus depending on the source redshift: GRBs at different distances could be used to disentangle these two effects.

At present, all the experimental data in the MeV-GeV range have been obtained only from satellite detectors, which however, due to their limited size and the fast decrease of the source energy spectra, hardly cover the energy region above 1 GeV. Ground-based experiments can easily reach much larger effective areas exploiting two different techniques, which correspond to two different types of detectors: Extensive Air Shower (EAS) arrays and Imaging Atmospheric Cherenkov Telescopes (IACTs). Concerning the latter, the huge telescope recently installed at the HESS site or the planned CTA observatory can allow the detection of γ -rays with energy as low as 20-30 GeV (Becherini et al. 2012; Bernlöhner et al. 2013), even if only at moderate zenith angles. However, IACTs can operate only during nights with good weather conditions and no or limited moon light, leading to a duty cycle

of 10-15%. Another disadvantage is given by the limited full field of view, about 5° , which requires a fast slew after an external alert in order to observe a GRB, but as pointed out by Gilmore et al. (2013), the MAGIC experience shows that most observations started after considerably longer times despite the instrument rapid slew capabilities, with only a minority occurring with total delay times of < 100 s, preventing the detection of short GRBs and the study of the very prompt phase of long GRBs. Due to the limited field of view, the prompt GRB location area must be quite small in order to be contained in it, but this is not the case for most of the GRBs detected by the Fermi-GBM. Until now, all the major Cherenkov telescope arrays (MAGIC, HESS, VERITAS) attempted to detect a GRB with a follow-up, but no robust positive result has been obtained and even with the new generation CTA only $\lesssim 1$ detection per year is expected (Gilmore et al. 2013).

On the contrary, EAS arrays have a large field of view (~ 2 sr) and a very high duty cycle (in principle 100%), however the requirement of a sufficient number of secondary particles in order to reconstruct the shower arrival direction and primary energy leads to an energy threshold of at least ~ 100 GeV. A possible technique to reduce the energy threshold of EAS detectors is working in scaler mode (Vernetto 2000) instead of shower mode, that is, recording the counting rates of the detector in search for an increase in coincidence with a burst detected by a different experiment. Even if this technique does not allow the reconstruction of the arrival direction and thus an independent search, it benefits from the large effective area and field of view and from the very low dead time with an energy threshold typically around 1 GeV, thus overlapping the highest energies investigated by satellites experiments. The resulting sensitivity is limited, but for GRBs observed at low zenith angles it is comparable to the highest fluxes measured by satellites.

The ARGO-YBJ detector has operated in scaler mode from December 17, 2004 to February 7, 2013. In this period a total of 206 GRBs (selected from the GCN Circulars

Archive¹, the Second Fermi GBM Gamma-Ray Burst Catalog (von Kienlin et al. 2014; Gruber et al. 2014) and the Fermi GBM Burst Catalog website²) in the field of view of the detector were investigated searching for an increase in the detector counting rates. No significant excess has been found and corresponding upper limits to the fluence and energy cutoff under different assumptions on the spectrum are presented and discussed in this paper. A detailed description of the scaler mode technique, including the effective area calculation for gamma-rays and protons, the comparison between measured and simulated counting rates, the long-term counting rate behaviour and the detector stability over short and long time periods, can be found in Aielli et al. (2008), while the analysis procedure is described in Aielli et al. (2009a) together with the results on the first sample of GRBs analysed. The GRB search can be done both in shower and scaler mode; here only the results obtained with the latter are presented and discussed. Shower mode results on a reduced sample of GRBs are given in Aielli et al. (2009b).

2. THE DETECTOR

The Astrophysical Radiation with Ground-based Observatory at YangBaJing (ARGO-YBJ) (Aielli et al. 2012) is an EAS detector located at an altitude of 4300 m a.s.l. (atmospheric depth 606 g cm^{-2}) at the YangBaJing Cosmic Ray Laboratory (30.11°N , 90.53°E) in Tibet, P.R. China. It is mainly devoted to γ -ray astronomy (Aielli et al. 2010; Bartoli et al. 2011, 2012a,b,c, 2013a,b) and cosmic ray physics (Aielli et al. 2009c, 2011; Bartoli et al. 2012d,e, 2013c). The detector is made of a single layer of Resistive Plate Chambers (RPCs), operated in streamer mode and grouped into 153 units named “clusters”,

¹http://gcn.gsfc.nasa.gov/gcn3_archive.html

²<http://heasarc.gsfc.nasa.gov/W3Browse/fermi/fermigbrst.html>

of size $5.7 \times 7.6 \text{ m}^2$ (Aielli et al. 2006). Each cluster is made by 12 RPCs ($1.23 \times 2.85 \text{ m}^2$) and each RPC is read out by 10 pads ($55.6 \times 61.8 \text{ cm}^2$), representing the space-time pixels of the detector. The clusters are disposed in a central full-coverage carpet (130 clusters on an area $74 \times 78 \text{ m}^2$ with $\sim 92\%$ of active surface) surrounded by a partially instrumented ($\sim 20\%$) area up to $100 \times 110 \text{ m}^2$, which increases the effective area and improves the reconstruction of the core location in shower mode.

In scaler mode the total counts are measured every 0.5 s: for each cluster the signal coming from its 120 pads is added up and put in coincidence in a narrow time window (150 ns), giving the counting rates for ≥ 1 , ≥ 2 , ≥ 3 , and ≥ 4 pads, which are read by four independent scaler channels. These counting rates are referred in the following as $C_{\geq 1}$, $C_{\geq 2}$, $C_{\geq 3}$, and $C_{\geq 4}$, respectively, and the corresponding rates are $\sim 40 \text{ kHz}$, $\sim 2 \text{ kHz}$, $\sim 300 \text{ Hz}$, and $\sim 120 \text{ Hz}$. Since for the GRB search in scaler mode the authentication is only given by a satellite detection, the stability of the detector and the probability that it mimics a true signal are crucial and have to be deeply investigated.

The main sources of counting rate variations are the pressure, acting on the shower development in the atmosphere, and the ambient temperature, acting on the detector efficiency. The time scale of both variations is much larger than the typical GRB duration (seconds to minutes), so they can be neglected provided that the behaviour of the single cluster counting rates is Poissonian. A secondary local effect is due to the radon contamination in the detector hall. Electrons and γ -rays, from short-lived radon daughters (mainly ${}_{82}^{214}\text{Pb}$, ${}_{83}^{214}\text{Bi}$, ${}_{84}^{214}\text{Po}$) produced in the radon decay chain, are expected from β decays and isotope de-excitations. It has been shown that they can influence the cluster counting rates at a level of a few per cent of the reference value. Even in this case the time variations are larger (hours) than the typical GRB duration and they can be neglected in the data processing (Bartoli et al. 2014; Giroletti et al. 2011).

A very rapid variation can be induced by nearby lightning. For this reason two electric field monitors *EFM-100*, located at opposite sides of the experimental hall, and a storm tracker *LD-250* (both devices by Boltek industries³) have been installed to check the electric field variations. Details of this study are widely discussed in Zhou et al. (2011).

3. DATA SELECTION AND ANALYSIS

The ARGO-YBJ detector was completed in spring 2007, however, thanks to its modularity, the data taking started already in November 2004 (corresponding to the launch of the Swift satellite), ending in February 2013, when the detector was definitively switched off. In this period a total of 223 GRBs, detected by satellite instruments, occurred inside the ARGO-YBJ field of view (zenith angle $\theta \leq 45^\circ$, corresponding to 1.84 sr). The present analysis was carried out on 206 of them, since the other GRBs occurred during periods when the detector was inactive or not properly working. Unlike Δt_{90} , defined as the time during which 90% of the GRB keV-MeV photons is detected, the redshift and the spectrum in the same energy range are not always measured due to the difficulties introduced in Section 1. The spectra measured by satellites can be fitted with a simple power law, a smooth double power law (Band or Smoothly Broken Power Law, SBPL (Kaneko et al. 2006)) or a Cutoff Power Law (CPL). Figure 1a shows the Δt_{90} distribution, with the dashed area on the left indicating the short (≤ 2 s) GRB population, while figure 1b gives the distribution of the fluences measured by the satellites, all normalized to the energy interval 15-150 keV. For 103 GRBs of our sample the simple power law spectral index in the keV-MeV region was measured by satellite detectors and the corresponding distribution (with a mean value $\langle \alpha \rangle = 1.6$) is shown in Fig. 1c. For 24 of them the redshift is also known and the

³<http://www.boltek.com/>

corresponding distribution is shown in Fig. 1d, being $\langle z \rangle = 2.1$ the mean value of this subset. The durations Δt_{90} and spectral indices α of GRBs with known redshift are pointed out in Fig. 1a and 1c, respectively, with a dashed area (coloured red in the online version). For this subset the mean value and width of the three distributions are compatible with those for the whole GRB sample. The detailed list of the 24 GRBs with known redshift is given in table 1, while table 2 reports the same information for the remaining 182 GRBs.

For each GRB the following standard procedure has been adopted: check of the detector stability, cluster selection by means of quality cuts and calculation of the significance of the coincident signal in the ARGO-YBJ detector. In order to extract the maximum information from the experimental data, two analyses have been implemented:

- coincidence search for each GRB;
- cumulative search for stacked GRBs.

Details on quality cuts and detector stability are carefully discussed in Aielli et al. (2008), while the background evaluation and significance calculation, as well as the analysis technique itself, are described in Aielli et al. (2009a).

3.1. *Coincidence search*

The counting rates of the clusters surviving the quality cuts (with an average efficiency over the whole data set $\sim 87\%$) are added up and the normalized fluctuation function

$$f = (c - b)/\sigma, \quad \sigma = \sqrt{b + b \frac{\Delta t_{90} [s]}{600}} \quad (1)$$

is used to evaluate the significance of the excess observed in coincidence with the satellite

detection, where c is the total number of counts in the Δt_{90} time window starting at t_0 (the trigger time) of the signal, both given by the satellite detector, and b is the number of counts in a fixed time interval of 300 s before and after the signal, normalized to the Δt_{90} time. This analysis can be done for the counting rates of all the multiplicities ≥ 1 , ≥ 2 , ≥ 3 , ≥ 4 and 1, 2, 3, where the counting rates C_i are obtained from the measured counting rates $C_{\geq i}$ using the relation:

$$C_i = C_{\geq i} - C_{\geq i+1} \quad (i = 1, 2, 3) \quad (2)$$

In the following, if not otherwise specified, all the results are for the counting rate C_1 , which corresponds to the minimum primary energy in the ARGO-YBJ scaler mode. The detector stability over short time periods is discussed in Aielli et al. (2008), showing that the poissonian behaviour of the distribution of the normalized fluctuations f is preserved provided that the total time window considered by the analysis (i.e., the signal interval Δt_{90} plus the background interval 2×300 s) is less than 30 minutes. This condition is satisfied for all GRBs included in our data sample, therefore no long time corrections of the counting rates has been applied. Even if the distributions of the single cluster counter rates for integrated times up to half an hour are Poissonian, this is not true for the sum of different clusters, which shows larger fluctuations. This effect has been carefully analysed and it was found due to the correlation between the counting rates of different clusters given by the air shower lateral distribution, i.e., counts in different clusters due to the same EAS are not independent. The resulting widening can be taken into account introducing a Fano factor F (Fano 1947):

$$\sigma^2 = F \sigma_p^2 \quad (3)$$

where σ_p^2 is the Poissonian variance equal to the mean value of the counting rate distribution

and σ^2 is the measured variance. The Fano factor increases with the number of detector units used and the integration time (i.e., the GRB duration) while decreases for a sparse detector layout, and its effect is to reduce the sensitivity by a factor \sqrt{F} . For each GRB the \sqrt{F} is listed in tables 1 and 2, and the mean value calculated over the whole data sample is $\langle \sqrt{F} \rangle = 2.22$. In order to take into account this effect and calculate properly the signal significance we studied the local fluctuation of the normalized function f (defined in equation 1) in an interval $\pm 12 h$ around the GRB trigger time and used equation (17) of Li & Ma (1983). Figure 2 (dark solid line) shows the distribution of the resulting significances for all the 206 GRBs. No significant excess is measured, the largest being 3.52σ for GRB080727C, with a post-trial chance probability of $4.5 \cdot 10^{-2}$. Since the long GRBs typically show a softer spectrum with a lower Band peak energy, the same distribution only for the 27 short GRBs is shown in the same figure 2 (dark dashed area, coloured red in the online version). Even in this case no significant excess is measured, the most significant event being GRB051114 with 3.37σ and a post-trial chance probability of $1.0 \cdot 10^{-2}$. For this GRB, since we expect a harder energy spectrum from short GRBs, we carried out the same analysis using the higher multiplicity channels C_2, C_3 and $C_{\geq 4}$, obtaining a significance of 1.16, 1.09 and 1.95σ , respectively.

Besides this search, a time window broader than Δt_{90} has been considered to take into account the possible high energy afterglow. Ghisellini et al. (2010) found that the flux of 8 among the 11 brightest bursts detected by Fermi-LAT above 100 MeV (in the first 13 months of operation) decays as a power law with a typical slope $t^{-1.5}$. In this analysis we assumed this trend in the afterglow phase ($t \geq \Delta t_{90}$) and a constant flux during the GRB prompt emission since we consider only the time-averaged behaviour:

$$\begin{aligned}
 A(t) &= A_0 & (t \leq \Delta t_{90}) \\
 A(t) &= A_0(t/\Delta t_{90})^{-3/2} & (t > \Delta t_{90})
 \end{aligned}
 \tag{4}$$

with A_0 corresponding to the mean flux during the low energy emission time Δt_{90} . With this assumption, 2/3 of the total emission comes after Δt_{90} . To search for such a delayed emission, a longer time interval $\Delta t'_{90}$ has to be used. Its value is chosen in order to maximize the signal significance. Assuming Poissonian fluctuations and introducing a mean background counting rate k in units of Δt_{90} , the significance is:

$$\sigma(t) = \frac{\int_0^t A(t)dt}{\sqrt{k \cdot t/\Delta t_{90}}} \quad (5)$$

The maximum of this function is at $t/\Delta t_{90} = 16/9$. In our case, since the fluctuations are not purely Poissonian and the Fano factor F depends on the integration time, we searched for a maximum significance of the modified function:

$$\sigma'(t) = \sigma(t)/\sqrt{F(t)} \quad (6)$$

with an iterative procedure, increasing for each GRB the time window by the minimum 0.5 s step. Then the Fano factor is calculated giving the resulting significance from equation (6). This procedure is repeated covering the time interval from Δt_{90} to $2\Delta t_{90}$. The significance curve in this time window is then fitted by a second-order polynomial and the $\Delta t'_{90}$ corresponding to its maximum is used instead of Δt_{90} for this extended search. Since the Fano factor increases with time, $\Delta t'_{90}$ is always shorter than the purely Poissonian value and certainly fall into the search interval. This procedure searches for a maximum in the $[\Delta t_{90} - 2\Delta t_{90}]$ range in steps of 0.5 s, therefore the analysis has been limited to GRBs with $\Delta t_{90} \geq 1.5$ s, allowing a second order fit of function (6). Moreover, for the longer GRBs the Fano factor is so big that the increase of Δt_{90} does not improve the sensitivity and a clear maximum cannot be found. For these events $\Delta t'_{90} = \Delta t_{90}$ has been used, since this is the value that maximizes the signal to noise ratio for a constant signal during Δt_{90} . The $\Delta t'_{90}$ obtained for the 185 GRBs with $\Delta t_{90} \geq 1.5$ s are listed in tables 1 and 2 (for 61 of them $\Delta t'_{90} = \Delta t_{90}$). The corresponding significance distribution is shown in figure 3. No

significant excess is found also in this case, the larger one being 3.52σ for GRB080727C, with a post-trial chance probability of $4.1 \cdot 10^{-2}$.

3.2. *Stacked analysis*

Besides the coincidence analysis for each GRB, a stacked analysis has been carried out in order to search for common features of all GRBs in *Time* or in *Phase*.

In the *Time* analysis the counting rates for all the GRBs, in 9 windows ($\Delta t = 0.5, 1, 2, 5, 10, 20, 50, 100$ and 200 s) starting at t_0 , have been added up in order to investigate a possible common duration of the high energy emission. A positive observation at a fixed Δt could be used as an alternative value to the observed Δt_{90} duration and a different way to look for a possible high energy delayed component. Since the bins are not independent, the distribution of the significances of the 9 time intervals is compared with random distributions obtained for starting times different from t_0 in a time interval ± 12 hr around the true GRB trigger time. Moreover, for the sample of GRBs with known redshift (with z ranging from 0.48 to 5.6) the time windows have been corrected for the cosmological dilation factor $(1 + z)$. The most significant excess (1.5σ) is observed for the sample of 182 GRBs with no redshift at $\Delta t = 0.5$ s with a chance probability of 0.60, while the analysis of the 24 GRBs with measured redshift led to a maximum significance of 0.7σ in the shorter time window ($\Delta t = 0.5$ s at $z=0$).

In the *Phase* analysis only 165 GRBs with duration $\Delta t_{90} \geq 5$ s have been added up scaling their duration to a common phase plot (i.e., 10 bins each sampling a 10% wide interval of Δt_{90} , being 0.5 s the minimum duration for the scaler mode data acquisition). This analysis should point out a common feature of all GRBs in case of a GeV emission correlated with the GRB duration at lower energy. Even in this case no excess is found,

and the most significant bin, corresponding to the phase $[0.7 - 0.8]$ of Δt_{90} , has a marginal significance of 1.78σ .

4. FLUENCE AND E_{CUT} UPPER LIMITS

The fluence upper limits can be derived in the $[1 - 100]$ GeV range from our experimental data and making some assumptions on the GRB primary spectrum. For this calculation we used the maximum number of counts at 99% confidence level (c.l.) following equation (6) of Helene (1983). The interaction of the GRB photons with the EBL results in e-pair production which originates a spectral cutoff. This effect depends on the GRB redshift, with a lower cutoff energy for more distant GRBs. For this reason, the most meaningful upper limits are obtained for the sample of 24 GRBs with known redshift (see table 1), while for the others (table 2) a value of $z=2$ and $z=0.6$ has been adopted for long and short GRBs, respectively, according to their measured distributions (Jakobsson et al. 2006; Berger et al. 2005; Berger 2014). For the differential spectral indexes we used two extrapolations to estimate the expected high energy fluence for each GRB: a) the spectral index α_{sat} measured by satellite detectors in the keV-MeV energy range (corresponding to the f_{sat} values in tables 1 and 2) and b) the conservative value $\alpha = -2.5$ ($f_{2.5}$ values in tables 1 and 2). For case a), when the Band or SBPL spectral features have been identified, the higher energy spectral index (i.e. above the peak in the keV-MeV region) has been used. These assumptions represent respectively the most and less favourable spectral index hypotheses. The absorption effect due to the EBL is taken into account using the model described in Kneiske et al. (2004) and applying an exponential cutoff to the spectrum according to the redshift. Figure 4 shows the 99% c.l. upper limits as a function of z for the GRBs with known redshift. For 5 of them, whose spectrum is best fitted by a CPL, only the upper limits for case b) are given.

For GRB090902B (which was the GRB in the ARGO-YBJ field of view with the highest energy photon detected) the fluence extrapolated from Fermi-LAT observations in the same energy range is shown. Only for this GRB the GeV spectral index measured by Fermi-LAT has been used and the dashed area in figure 4 has been obtained applying an energy cutoff to the GRB spectrum running from 30 GeV (about the maximum energy measured by Fermi-LAT) to 100 GeV. According to our calculation, in the case of a spectrum extending up to 100 GeV the extrapolated GRB fluence is just a factor 2.7 lower than our expected sensitivity. Due to the peculiar GeV emission of this GRB, the search has been done also in different time windows, in particular in coincidence with the extended Fermi-LAT emission [0 – 90 s], the maximum density of events with energy >1 GeV [6 – 26 s] and the time of the 33.4 GeV photon [82 – 83 s]. The resulting significances are -0.03 , 1.00 and -0.52σ , respectively.

A comparison between the expected fluence, obtained extrapolating the keV-MeV spectra measured by satellites and including the EBL absorption, and the fluence upper limit determined with the ARGO-YBJ scaler data has been done for the 19 GRBs with measured redshift and energy spectrum best fitted by a simple power law, excluding the 5 events which present a CPL spectrum. The result is shown in figure 5. The 7 points on the right side of the line *Upper Limit (UL) = Expected Fluence (EF)* (i.e. in the region where the upper limits are lower than the extrapolated fluences) indicate that, since the corresponding GRBs were not detected, the chosen extrapolation is not feasible up to our range [1 – 100 GeV] or a cutoff should be present in the high energy tail of the spectrum. Therefore, assuming the spectral index measured at low energies, the maximum cutoff energy has been estimated as follows. The extrapolated fluence is calculated together with the fluence upper limit as a function of the cutoff energy E_{cut} . If the two curves cross in the [2 – 100 GeV] interval, the intersection gives the upper limit to the cutoff energy. This is what happens to four of them (GRB050802, GRB081028A, GRB090809A

and GRB110128A), for which the knowledge of the redshift allows the estimation of the extragalactic absorption and hence a more accurate fluence upper limit and cutoff energy determination. For three of them (GRB071112C, GRB090424 and GRB130113B) the estimated E_{cut} upper limit is below 2 GeV: we can conclude that in these cases the low energy spectrum cannot be extended to the GeV region and some additional features occur in the keV-MeV range. The values obtained for E_{cut} are reported in the last column of table 1 and shown in figure 6 (triangles) as a function of the spectral index. The same calculation can be made for the GRBs with unknown redshift assuming for the EBL absorption $z=2$ and $z=0.6$ for long and short ones respectively and the resulting E_{cut} values are given in the last column of table 2 and shown in figure 6 (dots). More realistic models for the spectrum shape and/or different hypotheses on the photon spectral index in the GeV region can be considered. Since all the 7 GRBs falling on the right side of the $UL=EF$ line in Fig. 5 are long, we first assumed a Band spectrum with an E_{peak} value of 160 keV and a spectral index $\beta = -2.34$, corresponding to the mean peak energy and high energy slope for this class of GRBs (Nava et al. 2011). With this model all the 7 GRBs result under threshold (i.e., the extrapolated fluence is lower than our upper limit).

Another possibility is to suppose a fixed ratio between the GeV and keV-MeV fluences. The simultaneous observation of GRBs in these energy bands has been performed in the past by EGRET and BATSE onboard the CGRO satellite and more recently by Fermi-LAT and Fermi-GBM for a handful of events. As pointed out by Dermer et al. (2010), for long GRBs this ratio is close to 0.1 when the energy ranges considered to determine the fluence are 100 MeV - 10 GeV and 20 keV - 2 MeV. As the GeV spectral index we used a value -2, consistent with both EGRET and Fermi-LAT mean values. This high energy component represents a strong deviation with respect to the Band spectrum, increasing significantly the expected GeV fluence even if to a smaller extent than extrapolating the keV-MeV spectra. Also under these hypotheses all the 7 long GRBs fall on the left side of the $UL=EF$

line in Figure 5.

5. DISCUSSION AND CONCLUSIONS

The detection of high energy photons by the Fermi-LAT instrument clearly demonstrates that at least a small fraction of GRBs emits in the GeV range. The detected photons experience two main processes: generation at the source and propagation through the intergalactic medium. Several models have been proposed to explain the production of high energy photons in GRBs, but according to the standard fireball shock model they are essentially caused by internal or external shocks. Once produced, a fraction of these photons are converted into electron-positron pairs due to the interaction with low energy photons, mainly of the infrared-optical-ultraviolet cosmic background (EBL). This mechanism limits the photon mean free path and thus the visible horizon, which decreases with the energy up to $\sim 10^{15}$ eV, where the interaction with the Cosmic Microwave Background Radiation makes it smaller than the Galactic radius. The signal reaching the Earth is the final result of all these production and propagation mechanisms, bringing valuable information on all of them but at the same time difficult to separate. Features like the maximum energy as a function of the redshift, the photon index and other temporal and spectral characteristics, if seen with sufficient statistics, could discriminate between different mechanisms and shed light in this still largely unknown field. For these reasons the study of GRBs would greatly benefit from the contribution of ground-based detectors to the direct satellite measurements.

In this paper a search for GRBs in coincidence with satellite detections has been carried out using the complete ARGO-YBJ data set. During about 8 years a total of 206 GRBs has been analysed, producing the largest GRB sample ever studied using the scaler mode technique. In the search for GeV γ -rays in coincidence with the GRB satellite detections, no evidence of emission was found for any event both for the whole sample

and for separate analyses of the two populations of long and short GRBs. For GRBs with duration ≥ 1.5 s the search for a signal in a time window extended with respect to the low energy one has been carried out with similar results. The stacked search, both in time and phase, has shown no deviation from the statistical expectations. The subset of 24 GRBs with known redshift has been carefully analysed in terms of fluence and cutoff upper limits. For GRB090902B the fluence upper limit using the GeV spectral index is very close to the Fermi-LAT measurement (a factor 2.7 higher), supposing a high energy emission extending from the observed 30 GeV up to 100 GeV. This GRB was certainly our best candidate for a detection, however an area 7.2 times larger would have been necessary. For the other GRBs with known redshift, fluence upper limits as low as 2.9×10^{-5} erg cm $^{-2}$ in the 1-100 GeV energy range have been set, assuming an high energy spectral index equal to that measured by satellites. Under this hypothesis, for 7 of them an upper limit to the cutoff energy has also been determined, otherwise an average Band spectrum or a fixed ratio between the high and low energy fluences must be assumed.

The expected rate of GRBs which could be observed by the ARGO-YBJ experiment, based on the Swift satellite detections, was between 0.1 and 0.5 year $^{-1}$ (Aielli et al. 2008) and it should have doubled with the later launch of the Fermi satellite. The value of 0.3 year $^{-1}$ obtained for our 90% c.l. upper limit is close to our lower expectation partially because the predicted Fermi detection rate was overestimated and partially because the LAT-detected GRBs have a spectrum softer than presumed.

In the next future, three huge ground-based detectors could continue this search with improved sensitivity. HAWC, a water Cherenkov detector with a surface of 22000 m 2 is under construction in Mexico at an altitude of 4100 m a.s.l.. Its expected detection rate is 1.55 year $^{-1}$ for short GRBs and 0.25 year $^{-1}$ for long GRBs, mainly using the shower mode technique in the range 50-500 GeV (Taboada & Gilmore 2014). CTA will observe the night

sky detecting the atmospheric Cherenkov light. Its huge telescopes for the detection of low energy γ -rays have been designed also for a fast slewing, allowing a repointing time $\lesssim 100$ s. Apart from a very lucky serendipitous observation, the CTA search is limited to long GRBs after the very prompt phase, with an expected detection rate ranging from 0.6 to 2 year⁻¹ according to baseline or optimistic assumptions and with a strong dependence on the energy threshold (more than on the pointing delay) (Gilmore et al. 2013). GRB detection from ground via the water Cherenkov technique will also be possible with the proposed LHAASO experiment (Cui et al. 2014), whose detection rate has not yet been estimated. Thirty years after the first proposal by Morello et al. (1984), the first solid detection of a GRB from ground seems at hand.

This work is supported in China by NSFC (Grant No. 10120130794), the Chinese Ministry of Science and Technology, the Chinese Academy of Sciences, the Key Laboratory of Particle Astrophysics, CAS, and in Italy by the Istituto Nazionale di Fisica Nucleare (INFN). We also acknowledge the essential support of W.Y. Chen, G. Yang, X.F. Yuan, C.Y. Zhao, R. Assiro, B. Biondo, S. Bricola, F. Budano, A. Corvaglia, B. DAquino, R. Esposito, A. Innocente, A. Mangano, E. Pastori, C. Pinto, E. Reali, F. Taurino, and A. Zerbini in the installation, debugging, and maintenance of the detector.

REFERENCES

- Abdo, A. A., Ackermann M., Ajello M. et al. 2009a, *ApJ*, 706, L138
- Abdo, A. A., Ackermann M., Arimoto M. et al. 2009b, *Science*, 323, 1688
- Ackermann, M., Asano, K., Atwood, W. B. et al. 2010, *ApJ*, 716, 1178
- Ackermann, M., Ajello, M., Asano, K. et al. 2011, *ApJ*, 729, 114
- Ackermann, M., Ajello, M., Asano, K. et al. 2013, *ApJS*, 209, 11
- Ackermann, M., Ajello, M., Asano, K. et al. 2014, *Science*, 343, 42
- Aielli, G., Assiro, R., Bacci, C., et al. 2006, *Nucl. Instrum. Methods*, A562, 92
- Aielli, G., Bacci, C., Barone, F. et al. 2008, *Astropart. Phys.*, 30, 85
- Aielli, G., Bacci, C., Barone, F. et al. 2009a, *ApJ*, 699, 1281
- Aielli, G., Bacci, C., Bartoli, B. et al. 2009b, *Astropart. Phys.*, 32, 47
- Aielli, G., Bacci, C., Bartoli, B. et al. 2009c, *Phys. Rev. D*, 80, 092004
- Aielli, G., Bacci, C., Bartoli, B. et al. 2010, *ApJ*, 714, L208
- Aielli, G., Bacci, C., Bartoli, B. et al. 2011, *ApJ*, 729, 113
- Aielli, G., Bacci, C., Bartoli, B. et al. 2012, *Nucl. Instrum. Methods*, A661, S50
- Atwood, W. B., Baldini, L., Bregeon, J. et al. 2013, *ApJ*, 774, 76
- Band, D., Matteson, J., Ford, L. et al. 1993, *ApJ*, 413, 281
- Bartoli, B., Bernardini, P., Bi, X. J. et al. 2011, *ApJ*, 734, 110
- Bartoli, B., Bernardini, P., Bi, X. J. et al. 2012a, *ApJ*, 745, L22

- Bartoli, B., Bernardini, P., Bi, X. J. et al. 2012b, *ApJ*, 758, 2
- Bartoli, B., Bernardini, P., Bi, X. J. et al. 2012c, *ApJ*, 760, 110
- Bartoli, B., Bernardini, P., Bi, X. J. et al. 2012d, *Phys. Rev. D*, 85, 022002
- Bartoli, B., Bernardini, P., Bi, X. J. et al. 2012e, *Phys. Rev. D*, 85, 092005
- Bartoli, B., Bernardini, P., Bi, X. J. et al. 2013a, *ApJ*, 767, 99
- Bartoli, B., Bernardini, P., Bi, X. J. et al. 2013b, *ApJ*, 779, 27
- Bartoli, B., Bernardini, P., Bi, X. J. et al. 2013c, *Phys. Rev. D*, 88, 082001
- Bartoli, B., Bernardini, P., Bi, X. J. et al. 2014, *Radiation Measurements*, 68, 42
- Becherini, Y., Punch, M. & H.E.S.S. Collaboration 2012, *AIP Conf. Proc.*, 1505, 741
- Berger, E., Kulkarni, S. R., Fox, D. B. et al. 2005, *ApJ*, 634, 501
- Berger, E. 2014, *Annu. Rev. Astron. Astrophys.*, 52 (arXiv:1311.2603v1)
- Bernlöhr, K., Barnacka, A., Becherini, Y. et al. 2013, *Astropart. Phys.*, 43, 171
- Campana, S., Mangano, V., Blustin, A. J. et al. 2006, *Nature*, 442, 1008
- Costa, E., Frontera, F., Heise, J. et al. 1997, *Nature*, 387, 783
- Cui, S., Liu, Ye, Liu, Yujuan & Ma, X. 2014, *Astropart. Phys.*, 54, 86
- Dermer, C.D. & Fermi Collaboration 2010, *AIP Conf. Proc.*, 1279, 191
- Fan, Y. Z., Piran, T., Narayan, R. & Wei, D-M. 2008, *MNRAS*, 384, 1483
- Fano, U. 1947, *Phys. Rev.*, 72, 26

- Finke, J. D., Dermer, C. D. & Böttcher, M. 2008, in AIP Conf. Ser. 1000, eds. M. Galassi, D. Palmer, E. Fenimore, 385
- Gal-Yam, A., Moon, D.-S., Fox, D. B. et al. 2004, ApJ, 609, L59
- Ghirlanda, G., Ghisellini, G. & Nava, L. 2010, A&A, 510, L7
- Ghisellini, G., Ghirlanda, G., Nava, L. & Celotti, A. 2010, MNRAS, 403, 926
- Gilmore, R. C., Bouvier, A., Connaughton, V. et al. 2013, Experimental Astronomy 35, 413
- Giroletti, E., Bolognino, I., Cattaneo, C. et al. 2011, Proc. 32nd ICRC (Beijing), 1, 18
- Gruber, D., Goldstein, A., Weller von Ahlefeld, V. et al. 2014, ApJS, 211, 12
- Guetta, D., & Granot, J. 2003, ApJ, 585, 885
- Helene, O. 1983, Nucl. Instrum. Methods, 212, 319
- Jakobsson, P., Levan, A., Fynbo J. P. U. et al. 2006, A&A, 447, 897
- Kanbach, G., Bertsch, D. L., Favale, A. et al. 1988, Space Sci. Rev., 49, 69
- Kaneko, Y., Preece, R. D., Briggs, M. S. et al. 2006, ApJS, 166, 298
- Kneiske, T. M., Bretz, T., Mannheim, K. & Hartmann, D. H. 2004, A&A, 413, 807
- Kocevski, D., Vianello, G., Chiang, J. et al. 2013, GCN Circ. 14532
- Kumar, P., & Barniol Duran, R. 2010, MNRAS, 409, 226
- Li, T., & Ma, Y. 1983, ApJ, 272, 317
- Longo, F., Moretti, E., Nava, L. et al. 2012, A&A. 547, A95
- Meegan, C., Lichti, G., Bhat, P. N. et al. 2009, ApJ, 702, 791

- Morello, C., Periale, L., & Navarra, G. 1984, *Il Nuovo Cimento*, 7C, 6
- Nava, L., Ghirlanda, G., Ghisellini, G. & Celotti, A. 2011, *A&A*. 530, A21
- Rosswog, S., Ramirez-Ruiz, E. & Davies, M. B. 2003, *MNRAS*, 345, 1077
- Ruffert, M., & Janka, H.-Th. 1999, *A&A*, 344, 573
- Stanek, K. Z., Matheson, T., Garnavich, P.M. et al. 2003, *ApJ*, 591, L17
- Taboada, I. & Gilmore, R.C. 2014, *Nucl. Instrum. Methods*, A742, 276
- Tanvir, N. R., Levan, A.J., Fruchter, A. S. et al. 2013, *Nature*, 500, 547
- Vernetto, S. 2000, *Astropart. Phys.*, 13, 75
- Vianello, G., Desiante, R. & Longo, F. 2013, *GCN Circ.* 15357
- von Kienlin, A., Meegan, C. A., Paciesas, W. S. et al. 2014, *ApJS*, 211, 13
- Weiler, K. W., Panagia, N. & Montes, M. J. 2001, *ApJ*, 562, 670
- Wang, X. Y., Cheng, K. S., Dai, Z. G. & Lu, T. 2005, *A&A*. 439, 957
- Zhou, X. M., Ye, N., Zhu, F. R. et al. 2011, *Proc. 32nd ICRC (Beijing)*, 11, 287

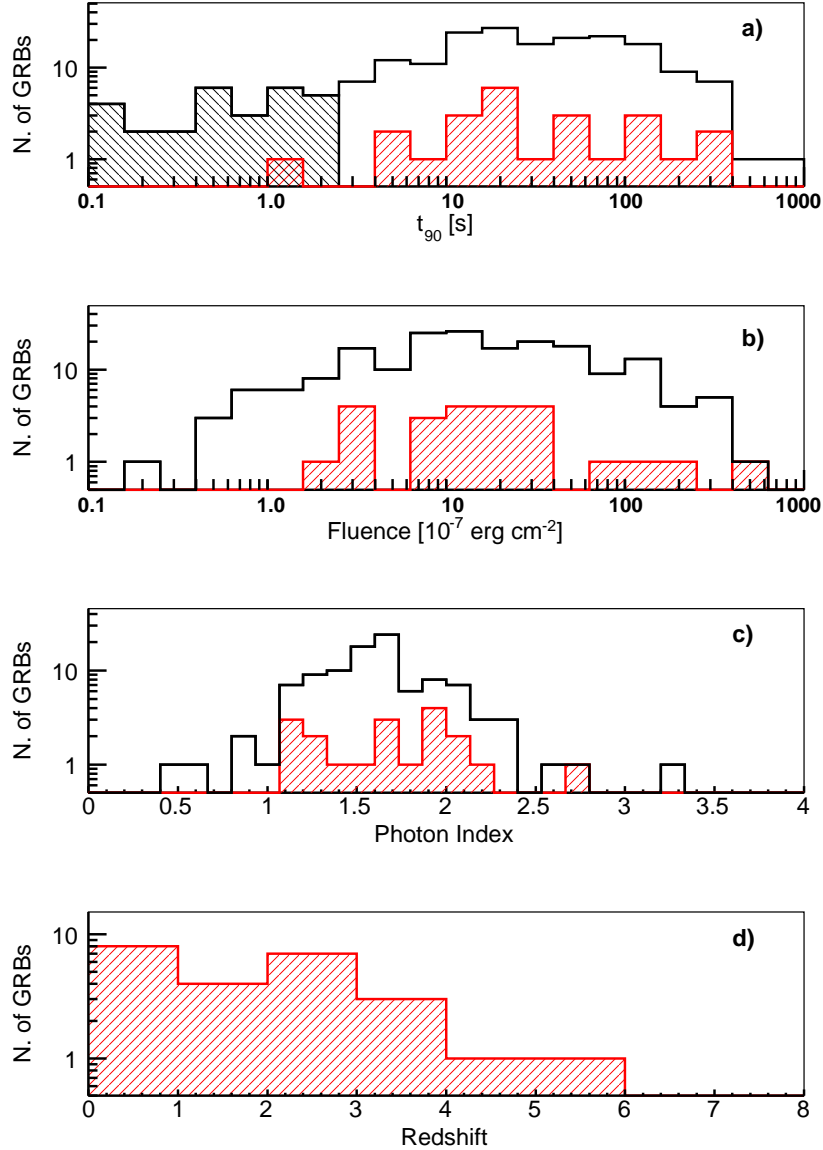


Fig. 1.— Details of the GRB sample analyzed in coincidence with ARGO-YBJ: a) Δt_{90} durations of the whole sample (solid line) and of the GRBs with known redshift (filled area); b) Fluences measured by satellites (all normalized to the energy range 15-150 keV) for the whole available sample (solid line) and for the events with known redshift (filled area); c) Photon index values in the keV-MeV band for the whole available sample (solid line) and for the events with known redshift (filled area); d) redshift values distribution. The dashed area on the left in plot a) indicates the short (≤ 2 s) GRB population.

(A color version of this figure is available in the online journal.)

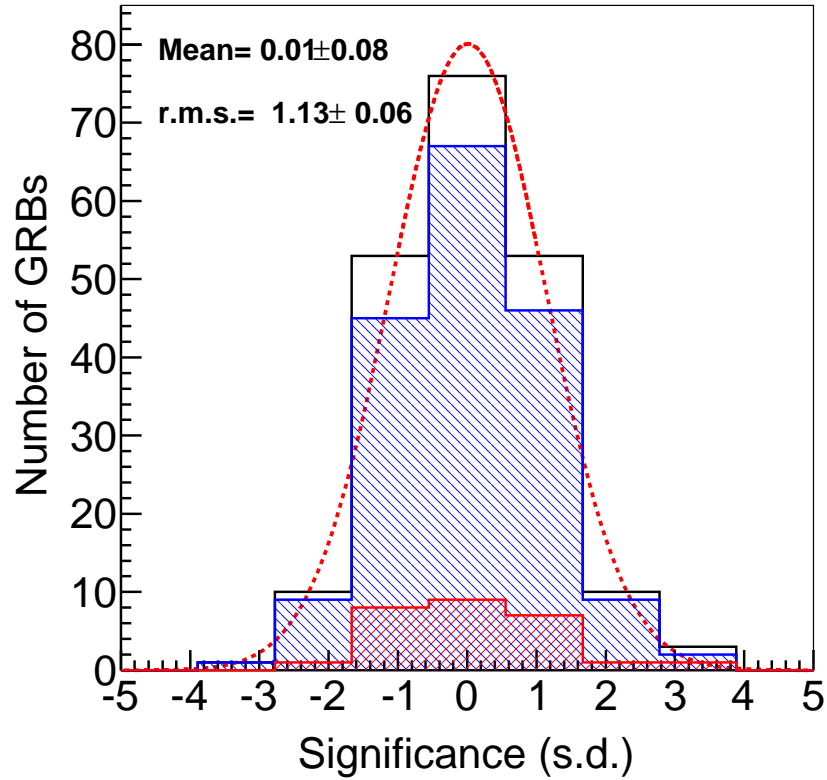


Fig. 2.— Distribution of the statistical significances of the 206 GRBs with respect to background fluctuations (dark solid line) compared with a free Gaussian fit (dotted line). Mean value and r.m.s. of the fit are shown. The light and dark dashed distributions refer to long and short GRBs, respectively.

(A color version of this figure is available in the online journal.)

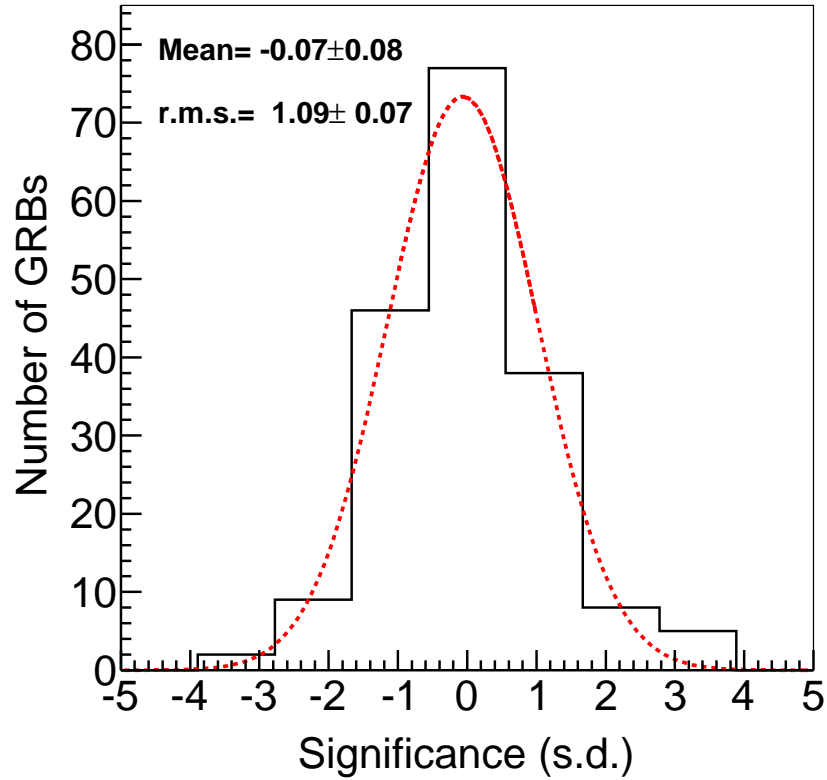


Fig. 3.— Distribution of the statistical significances of the 185 GRBs with $\Delta t_{90} \geq 1.5$ s with respect to background fluctuations (solid line) compared with a free Gaussian fit (dotted line) for the extended time window search (see text). Mean value and r.m.s. of the fit are shown.

(A color version of this figure is available in the online journal.)

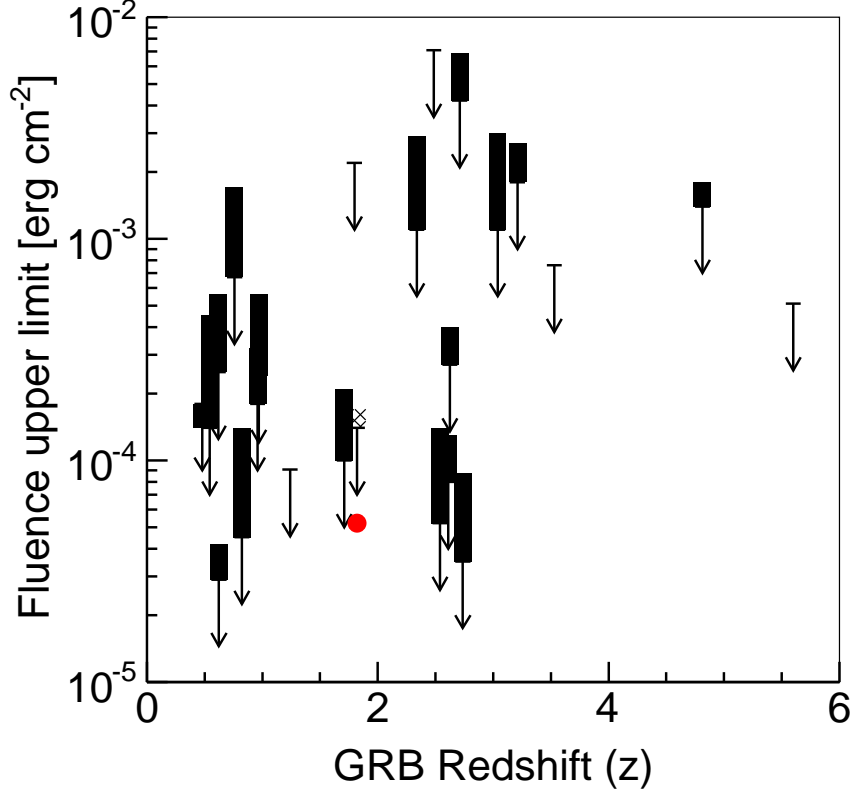


Fig. 4.— Fluence upper limits of GRBs in the 1-100 GeV interval as a function of redshift. The rectangles represent the values obtained with differential spectral indexes ranging from $\alpha = -2.5$ to the satellite measurement α_{sat} . The 5 arrows give the upper limits for the former case only, these GRBs being best fitted at lower energies with a cutoff power law spectrum. The dot shows the fluence extrapolated in the 1-100 GeV range from the Fermi-LAT observations of GRB090902B; only for this GRB the GeV spectral index has been used and the dashed area has been obtained applying an energy cutoff running from 30 to 100 GeV.

(A color version of this figure is available in the online journal.)

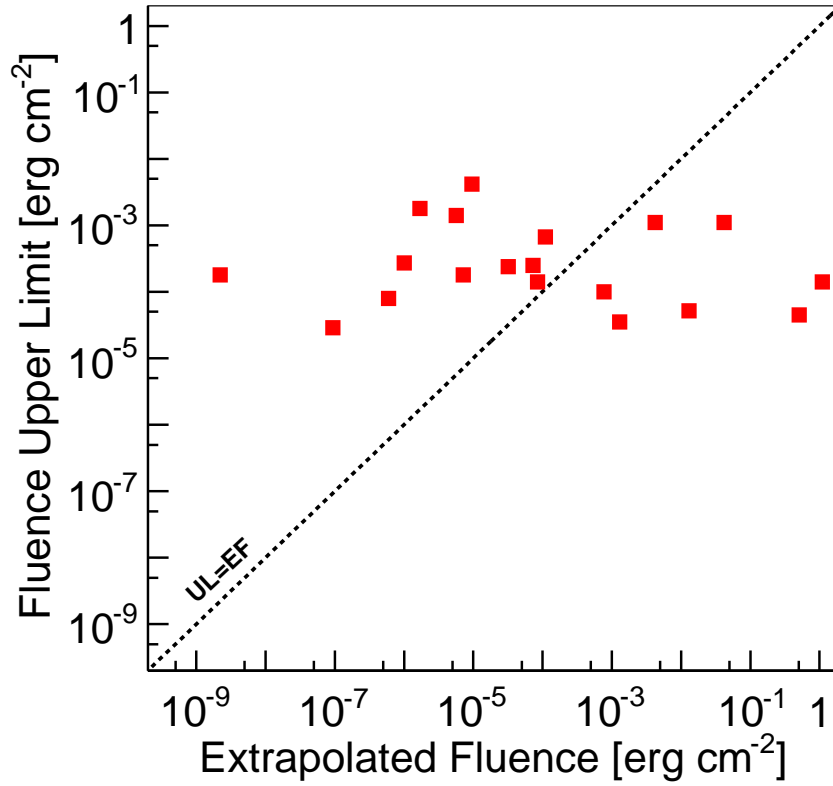


Fig. 5.— ARGO-YBJ upper limits (in the 1-100 GeV interval) vs. fluence extrapolation for GRBs with measured redshift and low energy power-law spectral index.

(A color version of this figure is available in the online journal.)

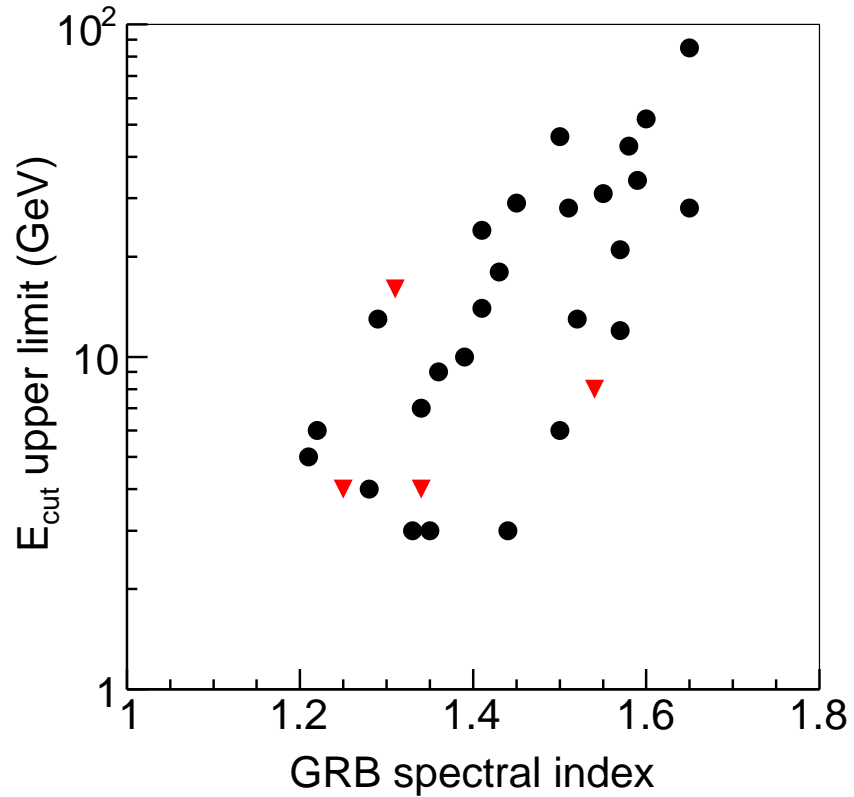


Fig. 6.— Cutoff energy upper limits as a function of the spectral index obtained by extrapolating the measured keV spectra. The values represented by the triangles are obtained taking into account extragalactic absorption at the known GRB redshift. For the other GRBs (dots) $z=2$ and $z=0.6$ are assumed for long e short ones, respectively.

(A color version of this figure is available in the online journal.)

Table 1. GRBs with measured redshift observed by ARGO-YBJ.

GRB	Satellite	Δt_{90}	$\Delta t'_{90}$	θ	z	\sqrt{F}	Spectral Index	A_{det}	σ	σ'	Fluence U.L. ^{a,c}	Fluence U.L. ^{b,c}	E_{cut} U.L. ^d
(1)	(2)	(s)	(s)	($^{\circ}$)	(6)	(7)	(α_{sat})	(m^2)	(10)	(11)	($erg\ cm^{-2}$) (f_{sat})	($erg\ cm^{-2}$) ($f_{2.5}$)	(GeV)
		(3)	(4)	(5)			(8)	(9)			(12)	(13)	(14)
050408	HETE	15	23.7	20.4	1.24	1.3	CPL	1560	-2.12	-2.90	—	$9.1 \cdot 10^{-5}$	-
050802	Swift	19	31.4	22.5	1.71	1.2	1.54	1516	0.19	-0.02	$1.0 \cdot 10^{-4}$	$2.1 \cdot 10^{-4}$	8
060115	Swift	139.6	139.6	16.6	3.53	3.0	CPL	3985	-1.02	-1.02	—	$7.6 \cdot 10^{-4}$	-
060526	Swift	298	298.0	31.7	3.21	3.9	2.01	4029	-1	-1.00	$1.8 \cdot 10^{-3}$	$2.7 \cdot 10^{-3}$	-
060714	Swift	115	115.0	42.8	2.71	4.9	1.93	5155	-0.61	-0.61	$4.2 \cdot 10^{-3}$	$6.9 \cdot 10^{-3}$	-
060927	Swift	22.5	31.3	31.6	5.6	1.6	CPL	5242	-0.14	-0.47	—	$5.1 \cdot 10^{-4}$	-
061110A	Swift	40.7	40.7	37.3	0.76	2.5	1.67	5545	0.01	0.01	$6.7 \cdot 10^{-4}$	$1.7 \cdot 10^{-3}$	-
071112C	Swift	15	22.0	18.4	0.82	1.5	1.09	5198	1.01	0.46	$4.5 \cdot 10^{-5}$	$1.4 \cdot 10^{-4}$	< 2
081028A	Swift	260	260.0	29.9	3.04	3.9	1.25	5805	0.37	0.37	$1.1 \cdot 10^{-3}$	$3.0 \cdot 10^{-3}$	4
090424	Swift	48	57.2	33.1	0.54	2.0	1.19	5762	0.6	0.71	$1.4 \cdot 10^{-4}$	$4.5 \cdot 10^{-4}$	< 2
090426	Swift	1.2	-	43.7	2.61	1.3	1.93	5805	-1.08	-	$8.0 \cdot 10^{-5}$	$1.3 \cdot 10^{-4}$	-
090529A	Swift	100	107.1	19.9	2.63	2.2	2	5892	-0.66	-0.83	$2.7 \cdot 10^{-4}$	$4.0 \cdot 10^{-4}$	-
090809A	Swift	5.4	7.9	34.2	2.74	1.5	1.34	5718	-1.12	-0.72	$3.5 \cdot 10^{-5}$	$8.8 \cdot 10^{-5}$	4
090902B	Fermi	25	36.6	23.1	1.82	1.7	1.94	5762	1.09	0.55	$1.4 \cdot 10^{-4}$	$2.2 \cdot 10^{-4}$	-
100302A	Swift	17.9	21.4	44.6	4.81	1.8	1.72	5675	0.04	0.03	$1.4 \cdot 10^{-3}$	$1.8 \cdot 10^{-3}$	-
100418A	Swift	7.0	10.9	18.7	0.62	1.5	2.16	5978	-1.33	-0.77	$2.9 \cdot 10^{-5}$	$4.2 \cdot 10^{-5}$	-
110106B	Swift	24.8	30.5	25.1	0.62	2.4	1.76	5675	2.25	2.09	$2.5 \cdot 10^{-4}$	$5.6 \cdot 10^{-4}$	-
110128A	Swift	30.7	30.7	43.2	2.34	2.3	1.31	5675	2.39	2.39	$1.1 \cdot 10^{-3}$	$2.9 \cdot 10^{-3}$	16
111211A	AGILE	15	18.4	20.3	0.48	1.8	2.77	5545	0.78	0.92	$1.8 \cdot 10^{-4}$	$1.4 \cdot 10^{-4}$	-
120326A	Swift	69.6	69.6	40.9	1.8	2.7	CPL	6021	-0.8	-0.80	—	$2.2 \cdot 10^{-3}$	-
120716A	IPN	230	230.0	35.7	2.49	3.9	CPL	5718	-0.57	-0.57	—	$7.1 \cdot 10^{-3}$	-
120722A	Swift	42.4	42.5	17.7	0.96	2.0	1.9	5848	1.23	1.17	$1.8 \cdot 10^{-4}$	$3.2 \cdot 10^{-4}$	-

Table 1—Continued

GRB	Satellite	Δt_{90}	$\Delta t'_{90}$	θ	z	\sqrt{F}	Spectral Index	A_{det}	σ	σ'	Fluence U.L. ^{a,c}	Fluence U.L. ^{b,c}	E_{cut} U.L. ^d
(1)	(2)	(s)	(s)	($^{\circ}$)	(6)	(7)	(α_{sat})	(m ²)	(10)	(11)	(erg cm ⁻²) (f_{sat})	(erg cm ⁻²) ($f_{2.5}$)	(GeV)
(1)	(2)	(3)	(4)	(5)	(6)	(7)	(8)	(9)	(10)	(11)	(12)	(13)	(14)
120907A	Swift	16.9	21.1	40.2	0.97	2.0	1.73	5892	-1.55	-1.49	$2.4 \cdot 10^{-4}$	$5.6 \cdot 10^{-4}$	-
130131B	Swift	4.3	6.2	27.2	2.54	1.6	1.15	5762	0.85	0.50	$5.2 \cdot 10^{-5}$	$1.4 \cdot 10^{-4}$	< 2

Note. —

^aUsing the spectrum determined by satellites.

^bAssuming a differential spectral index 2.5.

^c99% c.l.

^dDerived from the f_{sat} Fluence U.L. (see text).

^eFor high energy emission extending up to 30 GeV only (see text).

Column 1 is the GRB name corresponding to the detection date in UT (YYMMDD). Column 2 gives the satellite that detected the burst. Column 3 gives the burst duration Δt_{90} as measured by the respective satellite. Column 4 gives the extended burst duration $\Delta t'_{90}$. Column 5 gives the zenith angle with respect to the detector location. Column 6 gives the GRB redshift. Column 7 gives the square root of the Fano factor. Column 8 reports the spectral index: "CPL" means that the spectrum measured by the satellite is better fitted with a cutoff power law. Column 9 gives the detector active area for that burst. Columns 10 and 11 give the statistical significance of the on-source counts over the background for standard and extended burst duration. Columns 12 and 13 give the 99% confidence upper limits on the fluence between 1 and 100 GeV for spectral index of Column 8 and fixed value -2.5, respectively. Column 14 gives the cutoff upper limit, if any.

Table 2. GRBs with no measured redshift ($z = 2$ and $z=0.6$ are assumed for long and short GRBs, respectively) observed by ARGO-YBJ.

GRB	Satellite	Δt_{90}	$\Delta t'_{90}$	θ	\sqrt{F}	Spectral Index	A_{det}	σ	σ'	Fluence U.L. ^{a,c}	Fluence U.L. ^{b,c}	E_{cut} U.L. ^d
(1)	(2)	(s)	(s)	($^{\circ}$)	(6)	(α_{sat})	(m ²)	(9)	(10)	(erg cm ⁻²) (f_{sat})	(erg cm ⁻²) ($f_{2.5}$)	(GeV)
		(3)	(4)	(5)		(7)	(8)			(11)	(12)	(13)
041228	Swift	55.4	68.4	28.1	1.5	1.6	563	-0.01	-0.27	$5.8 \cdot 10^{-4}$	$1.3 \cdot 10^{-3}$	52
050509A	Swift	11.4	16.9	34	1.3	2.11	1473	0.62	0.88	$2.4 \cdot 10^{-4}$	$3.5 \cdot 10^{-4}$	-
050528	Swift	11.3	17.3	37.8	1.2	2.27	1473	0.71	0.04	$1.0 \cdot 10^{-3}$	$1.2 \cdot 10^{-3}$	-
051105A	Swift	0.1	-	28.5	1.2	1.22	3119	1.24	-	$1.4 \cdot 10^{-5}$	$4.5 \cdot 10^{-5}$	6
051114	Swift	2	3.2	32.8	1.4	1.21	3032	3.37	3.27	$5.0 \cdot 10^{-5}$	$1.6 \cdot 10^{-4}$	5
051227	Swift	114.6	114.6	22.8	2.9	1.45	2989	0.44	0.44	$4.8 \cdot 10^{-4}$	$1.1 \cdot 10^{-3}$	29
060105	Swift	54.4	54.4	16.3	2.7	1.07	3119	1.77	1.77	$3.3 \cdot 10^{-4}$	$8.7 \cdot 10^{-4}$	< 2
060111A	Swift	13	19.6	10.8	1.5	CPL	3206	0.39	0.54	-	$1.1 \cdot 10^{-4}$	-
060121	HETE	2	3.3	41.9	1.3	2.39	4159	0.6	0.58	$2.2 \cdot 10^{-4}$	$2.6 \cdot 10^{-4}$	-
060421	Swift	12	19.3	39.3	1.3	1.55	3855	-0.51	-0.62	$2.7 \cdot 10^{-4}$	$6.2 \cdot 10^{-4}$	31
060424	Swift	37.5	46.5	6.7	1.7	1.71	4072	0.12	-0.11	$9.5 \cdot 10^{-5}$	$1.8 \cdot 10^{-4}$	-
060427	Swift	64	76.6	32.6	1.8	1.87	4115	-0.13	-0.15	$3.4 \cdot 10^{-4}$	$6.0 \cdot 10^{-4}$	-
060510A	Swift	20.4	29.9	37.4	1.6	1.57	3899	2.42	2.31	$9.2 \cdot 10^{-4}$	$2.1 \cdot 10^{-3}$	21
060717	Swift	3	4.9	7.4	1.5	1.7	5155	1.58	0.33	$2.9 \cdot 10^{-5}$	$5.5 \cdot 10^{-5}$	-
060801	Swift	0.5	-	16.8	1.3	0.47	5415	0.81	-	$7.4 \cdot 10^{-6}$	$2.8 \cdot 10^{-5}$	< 2
060805B	IPN	8	12.1	29.1	1.5	2.52	5285	-0.45	-0.17	$1.3 \cdot 10^{-4}$	$1.3 \cdot 10^{-4}$	-
060807	Swift	54	54.0	12.4	2.6	1.58	5155	0.78	0.78	$1.7 \cdot 10^{-4}$	$3.4 \cdot 10^{-4}$	43
061028	Swift	106	106.0	42.5	1.9	1.73	5458	-3.33	-3.33	$4.7 \cdot 10^{-4}$	$9.5 \cdot 10^{-4}$	-
061122	Integral	18	18.0	33.5	3.9	CPL	5025	0.6	0.67	-	$7.4 \cdot 10^{-4}$	-
070201	IPN	0.3	-	20.6	1.3	CPL	5242	-1.21	-	-	$1.1 \cdot 10^{-5}$	-
070219	Swift	16.6	20.0	39.3	1.8	1.78	4982	-0.71	-0.76	$4.2 \cdot 10^{-4}$	$8.0 \cdot 10^{-4}$	-
070306	Swift	209.5	209.5	19.9	3.4	1.66	2513	-0.83	-0.83	$7.0 \cdot 10^{-4}$	$1.3 \cdot 10^{-3}$	-

Table 2—Continued

GRB	Satellite	Δt_{90}	$\Delta t'_{90}$	θ	\sqrt{F}	Spectral Index	A_{det}	σ	σ'	Fluence U.L. ^{a,c}	Fluence U.L. ^{b,c}	E_{cut} U.L. ^d
(1)	(2)	(s)	(s)	($^{\circ}$)	(6)	(α_{sat})	(m ²)	(9)	(10)	(erg cm ⁻²) (f_{sat})	(erg cm ⁻²) ($f_{2.5}$)	(GeV)
(1)	(2)	(3)	(4)	(5)	(6)	(7)	(8)	(9)	(10)	(11)	(12)	(13)
070531	Swift	44.5	58.0	44.3	1.6	1.41	2816	0.59	0.65	$9.1 \cdot 10^{-4}$	$2.3 \cdot 10^{-3}$	24
070615	Integral	30	37.1	37.6	1.7	-	5328	1.81	2.21	—	$2.0 \cdot 10^{-3}$	-
071013	Swift	26	32.1	13.3	1.9	1.6	4765	-0.06	-0.21	$6.7 \cdot 10^{-5}$	$1.4 \cdot 10^{-4}$	-
071101	Swift	9	14.1	32.8	1.4	2.25	3596	1.01	0.53	$2.0 \cdot 10^{-4}$	$2.5 \cdot 10^{-4}$	-
071104	AGILE	12	16.7	19.9	1.9	-	4029	-0.07	-0.24	—	$1.5 \cdot 10^{-4}$	-
071118	Swift	71	71.0	41.2	2.8	1.63	5025	0.54	0.54	$1.8 \cdot 10^{-3}$	$3.9 \cdot 10^{-3}$	-
080328	Swift	90.6	90.6	37.2	2.7	1.52	6065	-1.19	-1.19	$1.0 \cdot 10^{-3}$	$2.4 \cdot 10^{-3}$	13
080602	Swift	74	74.0	42	2.4	1.43	5762	1.24	1.24	$1.5 \cdot 10^{-3}$	$3.7 \cdot 10^{-3}$	18
080613B	Swift	105	105.0	39.2	2.6	1.39	5718	0.65	0.65	$1.7 \cdot 10^{-3}$	$4.3 \cdot 10^{-3}$	10
080714B	Fermi	5.4	8	24.4	1.5	CPL	5805	-0.34	-0.32	—	$5.8 \cdot 10^{-5}$	-
080727C	Swift	79.7	79.7	34.5	2.1	CPL	5415	3.52	3.52	—	$1.6 \cdot 10^{-3}$	-
080730A	Fermi	17.4	25.5	31.2	1.5	1.96	5545	-0.26	-0.87	$1.2 \cdot 10^{-4}$	$2.0 \cdot 10^{-4}$	-
080822B	Swift	64	65.8	40.3	2.4	2.54	5762	-1.84	-1.93	$1.6 \cdot 10^{-3}$	$1.5 \cdot 10^{-3}$	-
080830	Fermi	45	45.0	37.1	2.1	1.69	5805	-0.04	-0.04	$8.5 \cdot 10^{-4}$	$1.8 \cdot 10^{-3}$	-
080903	Swift	66	66.0	21.5	2.3	CPL	5588	-1.33	-1.33	—	$2.6 \cdot 10^{-4}$	-
081025	Swift	23	32.6	30.5	1.6	1.12	5718	-0.48	-0.95	$7.9 \cdot 10^{-5}$	$2.3 \cdot 10^{-4}$	< 2
081102B	Fermi	2.2	3.3	27.8	1.4	1.07	5762	0.02	-0.64	$2.3 \cdot 10^{-5}$	$6.8 \cdot 10^{-5}$	< 2
081105	IPN	10	15.1	36.7	1.5	-	5718	-0.77	-0.82	—	$4.7 \cdot 10^{-4}$	-
081122	Fermi	26	30.7	8.3	1.8	2.24	4289	-2.03	-2.07	$6.5 \cdot 10^{-5}$	$8.1 \cdot 10^{-5}$	-
081128	Swift	100	100.0	31.8	3.6	CPL	5242	-0.63	-0.63	—	$1.1 \cdot 10^{-3}$	-
081130B	Fermi	12	14.7	28.6	2.3	CPL	5978	-0.05	0.03	—	$2.6 \cdot 10^{-4}$	-
081215A	Fermi	7.7	10.3	35.9	1.9	2.20	5762	-0.15	0.26	$4.5 \cdot 10^{-4}$	$6.0 \cdot 10^{-4}$	-

Table 2—Continued

GRB	Satellite	Δt_{90}	$\Delta t'_{90}$	θ	\sqrt{F}	Spectral Index	A_{det}	σ	σ'	Fluence U.L. ^{a,c}	Fluence U.L. ^{b,c}	E_{cut} U.L. ^d
(1)	(2)	(s)	(s)	($^{\circ}$)	(6)	(α_{sat})	(m ²)	(9)	(10)	(erg cm ⁻²) (f_{sat})	(erg cm ⁻²) ($f_{2.5}$)	(GeV)
(1)	(2)	(3)	(4)	(5)	(6)	(7)	(8)	(9)	(10)	(11)	(12)	(13)
090107A	Swift	12.2	14.7	40.1	2.0	1.69	5762	-1.12	-1.59	$3.0 \cdot 10^{-4}$	$6.2 \cdot 10^{-4}$	-
090118	Swift	16	21.1	13.4	1.9	1.35	5805	-1.62	-1.45	$2.7 \cdot 10^{-5}$	$6.3 \cdot 10^{-5}$	3
090301	Swift	41.0	41.0	14.2	2.5	CPL	5805	0.73	0.73	—	$2.6 \cdot 10^{-4}$	-
090301B	Fermi	28	29.8	24.3	2.2	<i>1.93</i>	5892	-2.2	-2.15	$7.8 \cdot 10^{-5}$	$1.2 \cdot 10^{-4}$	-
090306B	Swift	20.4	20.4	38.5	2.3	CPL	5805	-0.65	-0.65	—	$1.1 \cdot 10^{-3}$	-
090320B	Fermi	52	60.1	29	2.1	CPL	5892	-0.25	0.04	—	$4.9 \cdot 10^{-4}$	-
090328B	Fermi	0.32	-	15.5	1.3	<i>2.48</i>	5848	0.48	-	$1.6 \cdot 10^{-5}$	$1.7 \cdot 10^{-5}$	-
090403	Fermi	16	21.5	28.5	1.8	-	6021	0.65	1.16	—	$2.9 \cdot 10^{-4}$	-
090407	Swift	310	310.0	45	3.4	1.73	6021	1.53	1.53	$6.7 \cdot 10^{-3}$	$1.4 \cdot 10^{-2}$	-
090417B	Swift	260	260.0	37.2	4.0	1.85	5978	0.64	0.64	$6.2 \cdot 10^{-3}$	$1.1 \cdot 10^{-2}$	-
090425	Fermi	72	92.0	44.6	1.9	<i>2.03</i>	5848	1.7	2.13	$2.1 \cdot 10^{-3}$	$3.3 \cdot 10^{-3}$	-
090511	Fermi	14	17.9	39	1.7	CPL	5848	0.35	0.09	—	$8.8 \cdot 10^{-4}$	-
090520A	Swift	20	25.1	42.2	2.0	0.8	5892	-0.65	-0.57	$2.6 \cdot 10^{-4}$	$9.2 \cdot 10^{-4}$	< 2
090529C	Fermi	10.4	15.6	22.1	1.4	<i>2.1</i>	5892	1.16	1.34	$8.8 \cdot 10^{-5}$	$1.2 \cdot 10^{-4}$	-
090617	Fermi	0.45	-	16.1	1.4	<i>2.00</i>	5978	0.32	-	$1.4 \cdot 10^{-5}$	$2.4 \cdot 10^{-5}$	-
090621B	Swift	0.14	-	40.5	1.3	0.82	5935	0.5	-	$2.4 \cdot 10^{-5}$	$1.0 \cdot 10^{-4}$	< 2
090704B	Fermi	19.5	27.6	4.3	1.7	1.65	5848	-0.66	-0.37	$3.7 \cdot 10^{-5}$	$7.2 \cdot 10^{-5}$	28
090712	Swift	145	145.0	10.7	3.7	1.33	5025	-0.04	-0.04	$2.9 \cdot 10^{-4}$	$6.9 \cdot 10^{-4}$	3
090730A	Fermi	9.1	14.6	4.4	1.4	CPL	5805	0.52	-0.46	—	$5.9 \cdot 10^{-5}$	-
090807A	Swift	140.8	140.8	19.9	3.1	2.25	5935	-0.76	-0.76	$5.1 \cdot 10^{-4}$	$6.3 \cdot 10^{-4}$	-
090807B	Fermi	3	5.2	29.3	1.3	<i>2.4</i>	5978	-1.14	-2.69	$5.1 \cdot 10^{-5}$	$5.6 \cdot 10^{-5}$	-
090811A	Fermi	14.8	21.7	23.1	1.7	CPL	5805	-0.46	-0.29	—	$1.1 \cdot 10^{-4}$	-

Table 2—Continued

GRB	Satellite	Δt_{90}	$\Delta t'_{90}$	θ	\sqrt{F}	Spectral Index	A_{det}	σ	σ'	Fluence U.L. ^{a,c}	Fluence U.L. ^{b,c}	E_{cut} U.L. ^d
(1)	(2)	(s)	(s)	($^{\circ}$)	(6)	(α_{sat})	(m ²)	(9)	(10)	(erg cm ⁻²) (f_{sat})	(erg cm ⁻²) ($f_{2.5}$)	(GeV)
(1)	(2)	(3)	(4)	(5)	(6)	(7)	(8)	(9)	(10)	(11)	(12)	(13)
090814B	Integral	50	50.5	31.1	2.2	-	5805	-1.05	-1.03	—	$4.2 \cdot 10^{-4}$	-
090817	Integral	220	220.0	14.6	2.9	<i>2.2</i>	5892	-0.77	-0.77	$4.0 \cdot 10^{-4}$	$5.2 \cdot 10^{-4}$	-
090820A	Fermi	30	41.2	17.1	1.7	<i>2.61</i>	5935	0.25	0.39	$2.0 \cdot 10^{-4}$	$1.9 \cdot 10^{-4}$	-
090824A	Fermi	59.9	69	30.8	1.7	2.01	5805	0.71	0.49	$3.7 \cdot 10^{-4}$	$5.8 \cdot 10^{-4}$	-
090831A	Fermi	53	67.9	35.8	2.8	CPL	4679	0.59	0.24	—	$3.4 \cdot 10^{-3}$	-
090904A	Swift	122	164.8	21.9	1.9	2.01	5805	0.37	2.97	$3.4 \cdot 10^{-4}$	$5.1 \cdot 10^{-4}$	-
090904C	Fermi	38.4	46.6	33	1.9	CPL	5978	-1.66	-1.87	—	$2.6 \cdot 10^{-4}$	-
091106A	Fermi	14.6	19.4	30.2	2	CPL	5762	-0.17	-0.32	—	$2.5 \cdot 10^{-4}$	-
091202	Integral	45	45.0	33.2	3.2	-	5415	-0.64	-0.64	—	$6.5 \cdot 10^{-4}$	-
091215A	Fermi	4.4	6.1	25.4	1.5	1.65	5285	-1.36	-0.95	$3.5 \cdot 10^{-5}$	$7.4 \cdot 10^{-5}$	85
091224A	Fermi	0.8	-	16.8	1.3	1.21	5068	-1.56	-	$4.7 \cdot 10^{-6}$	$1.4 \cdot 10^{-5}$	< 2
091227A	Fermi	21.9	23.6	27.9	2.1	CPL	5242	0.85	1.09	—	$4.4 \cdot 10^{-4}$	-
100111A	Swift	12.9	12.9	21.5	2.7	1.69	5458	-1.03	-1.03	$7.5 \cdot 10^{-5}$	$1.4 \cdot 10^{-4}$	-
100115A	Swift	3	4.7	32.6	1.5	-	5588	-0.29	-0.14	—	$8.4 \cdot 10^{-5}$	-
100122A	Fermi	6.6	9.3	33.1	1.6	<i>2.31</i>	5805	0.84	0.92	$1.4 \cdot 10^{-4}$	$1.7 \cdot 10^{-4}$	-
100131A	Fermi	6.2	9.0	14	1.4	<i>2.21</i>	5588	1.01	1.16	$4.8 \cdot 10^{-5}$	$6.1 \cdot 10^{-5}$	-
100206A	Swift	0.12	-	26.8	1.2	0.63	4245	0.9	-	$8.5 \cdot 10^{-6}$	$3.4 \cdot 10^{-5}$	< 2
100210A	Fermi	29.2	29.2	24.9	2.4	1.71	5675	0.25	0.25	$1.5 \cdot 10^{-4}$	$2.7 \cdot 10^{-4}$	-
100225B	Fermi	32.0	38.4	22.1	1.9	1.51	5892	-1.83	-2.24	$5.9 \cdot 10^{-5}$	$1.2 \cdot 10^{-4}$	28
100225D	Fermi	4.5	7.1	8.4	1.5	CPL	5805	-1.19	-1.11	—	$2.8 \cdot 10^{-5}$	-
100424A	Swift	104	104.0	33.4	2.4	1.83	6021	0.41	0.41	$5.3 \cdot 10^{-4}$	$9.6 \cdot 10^{-4}$	-
100503A	Fermi	129.5	129.5	26.4	4.5	CPL	6065	0.09	0.09	—	$1.9 \cdot 10^{-3}$	-

Table 2—Continued

GRB	Satellite	Δt_{90}	$\Delta t'_{90}$	θ	\sqrt{F}	Spectral Index	A_{det}	σ	σ'	Fluence U.L. ^{a,c}	Fluence U.L. ^{b,c}	E_{cut} U.L. ^d
(1)	(2)	(s)	(s)	($^{\circ}$)	(6)	(α_{sat})	(m ²)	(9)	(10)	(erg cm ⁻²) (f_{sat})	(erg cm ⁻²) ($f_{2.5}$)	(GeV)
(1)	(2)	(3)	(4)	(5)	(6)	(7)	(8)	(9)	(10)	(11)	(12)	(13)
100513B	Fermi	11.1	16.2	38.7	1.6	CPL	5502	1.16	1.17	—	$9.0 \cdot 10^{-4}$	-
100522A	Swift	35.3	46.0	27.7	1.7	1.89	4679	0.86	0.62	$2.8 \cdot 10^{-4}$	$4.9 \cdot 10^{-4}$	-
100525A	Fermi	1.5	2.5	13.7	1.4	CPL	5892	0.65	-0.16	—	$2.2 \cdot 10^{-5}$	-
100526A	Swift	102	102.7	9.5	2.5	1.83	5935	-0.72	-0.79	$1.7 \cdot 10^{-4}$	$2.8 \cdot 10^{-4}$	-
100527A	Fermi	184.6	297.4	33.3	2.2	CPL	5935	2.33	3.4	—	$2.6 \cdot 10^{-3}$	-
100530A	Fermi	3.3	5	39	1.4	1.66	6108	1.15	0.14	$1.8 \cdot 10^{-4}$	$3.9 \cdot 10^{-4}$	-
100614B	Fermi	172.3	197.9	43.2	2.4	CPL	5978	-0.24	-0.86	—	$4.0 \cdot 10^{-3}$	-
100621C	Fermi	1.0	-	31.5	1.3	-	5762	0.71	-	—	$4.3 \cdot 10^{-5}$	-
100625B	Fermi	29.2	36.4	15.4	1.7	CPL	5458	1.07	0.55	—	$2.5 \cdot 10^{-4}$	-
100706A	Fermi	0.1	-	18.3	1.3	1.28	5675	0.39	-	$5.6 \cdot 10^{-6}$	$1.6 \cdot 10^{-5}$	4
100713A	Integral	20	23.1	12.5	2.6	-	5848	0.43	0.37	—	$1.7 \cdot 10^{-4}$	-
100714B	Fermi	5.6	8.7	39.9	1.5	CPL	5502	-0.81	-0.07	—	$3.6 \cdot 10^{-4}$	-
100718A	Fermi	38.7	47.6	16.7	2.1	CPL	5632	-0.52	-0.47	—	$2.2 \cdot 10^{-4}$	-
100728A	Swift	198.5	198.5	44.8	2.6	1.18	6021	0.49	0.49	$2.0 \cdot 10^{-3}$	$5.8 \cdot 10^{-3}$	< 2
100902A	Swift	428.8	428.8	37	5.0	1.98	5415	0.41	0.41	$1.2 \cdot 10^{-2}$	$1.9 \cdot 10^{-2}$	-
100929A	Fermi	8.2	12.4	34.9	1.4	1.36	5892	-0.38	-0.68	$4.8 \cdot 10^{-5}$	$1.2 \cdot 10^{-4}$	9
100929B	Fermi	4.6	7.2	27.2	1.5	1.54	5848	-0.68	-0.61	$4.0 \cdot 10^{-5}$	$9.1 \cdot 10^{-5}$	-
101003A	Fermi	10.0	15.3	30.8	1.5	CPL	5892	-0.28	-0.11	—	$1.5 \cdot 10^{-4}$	-
101008A	Swift	104	104.0	25.6	2.4	1.59	5848	0.3	0.30	$4.5 \cdot 10^{-4}$	$9.8 \cdot 10^{-4}$	-
101101A	Fermi	3.3	4.8	25.5	1.5	2.02	5935	-0.02	0.57	$5.5 \cdot 10^{-5}$	$8.6 \cdot 10^{-5}$	-
101107A	Fermi	375.8	375.8	25.8	3	CPL	5892	3	3	—	$6.4 \cdot 10^{-3}$	-
101112B	Fermi	82.9	82.9	39.9	3.3	CPL	5805	-0.95	-0.95	—	$3.0 \cdot 10^{-3}$	-

Table 2—Continued

GRB	Satellite	Δt_{90}	$\Delta t'_{90}$	θ	\sqrt{F}	Spectral Index	A_{det}	σ	σ'	Fluence U.L. ^{a,c}	Fluence U.L. ^{b,c}	E_{cut} U.L. ^d
(1)	(2)	(s)	(s)	($^\circ$)	(6)	(α_{sat})	(m ²)	(9)	(10)	(erg cm ⁻²) (f_{sat})	(erg cm ⁻²) ($f_{2.5}$)	(GeV)
(1)	(2)	(3)	(4)	(5)	(6)	(7)	(8)	(9)	(10)	(11)	(12)	(13)
101123A	Fermi	105	105.0	23.7	3.5	<i>2.14</i>	5978	-1.79	-1.79	$3.1 \cdot 10^{-4}$	$4.1 \cdot 10^{-4}$	-
101202A	Fermi	18.4	26.3	38	1.5	1.62	5848	-0.61	-0.38	$3.0 \cdot 10^{-4}$	$6.6 \cdot 10^{-4}$	-
101208A	Fermi	0.2	-	37.3	1.2	CPL	3899	-0.42	-	-	$8.9 \cdot 10^{-5}$	-
101224A	Swift	0.2	-	22.6	1.3	CPL	5675	-0.67	-	-	$1.2 \cdot 10^{-5}$	-
101231A	Fermi	23.6	23.6	24	2.5	<i>2.44</i>	5675	-0.58	-0.58	$1.9 \cdot 10^{-4}$	$1.9 \cdot 10^{-4}$	-
110101A	Fermi	3.6	5	6.4	1.8	1.51	5848	0.21	0.23	$2.1 \cdot 10^{-5}$	$4.4 \cdot 10^{-5}$	-
110106A	Swift	4.3	6.0	34.8	1.6	1.71	5588	-1.28	-1.71	$3.8 \cdot 10^{-5}$	$7.6 \cdot 10^{-5}$	-
110206B	Fermi	12.3	17.8	43.4	1.5	1.55	5458	-0.07	0.13	$2.7 \cdot 10^{-4}$	$6.2 \cdot 10^{-4}$	-
110210A	Swift	233	233.0	23	7.2	1.73	5762	1.15	1.15	$1.9 \cdot 10^{-3}$	$3.4 \cdot 10^{-3}$	-
110220A	Fermi	33.0	33	31	2.2	CPL	5935	1.83	1.83	-	$7.4 \cdot 10^{-4}$	-
110226A	Fermi	14.1	17.7	37	1.8	CPL	5805	-0.89	-1.09	-	$6.4 \cdot 10^{-4}$	-
110312A	Swift	28.7	30.3	37.2	2.2	2.32	5805	0.3	0.21	$1.3 \cdot 10^{-3}$	$1.5 \cdot 10^{-3}$	-
110315A	Swift	77	85.9	19.3	2.9	1.77	5112	-2.26	-2.58	$1.6 \cdot 10^{-4}$	$2.9 \cdot 10^{-4}$	-
110328B	Fermi	40	40.0	20.8	2.6	3.31	6151	1.34	1.34	$7.4 \cdot 10^{-4}$	$4.4 \cdot 10^{-4}$	-
110401A	Fermi	2	3.5	15.2	1.3	<i>2.36</i>	5675	-0.94	-0.35	$1.9 \cdot 10^{-5}$	$2.2 \cdot 10^{-5}$	-
110406A	Integral	8	12.7	31.1	1.5	<i>2.30</i>	6108	-0.1	0.07	$1.1 \cdot 10^{-4}$	$1.3 \cdot 10^{-4}$	-
110414A	Swift	152.0	152.0	44.1	3.3	1.7	6021	-0.92	-0.92	$2.0 \cdot 10^{-3}$	$4.2 \cdot 10^{-3}$	-
110517A	Fermi	0.6	-	29.5	1.3	1.29	5198	2.55	-	$2.1 \cdot 10^{-5}$	$6.8 \cdot 10^{-5}$	13
110605A	Fermi	82.7	82.7	33.8	3	<i>2.20</i>	6065	-0.01	-0.01	$7.0 \cdot 10^{-4}$	$9.3 \cdot 10^{-4}$	-
110605B	Fermi	1.5	2.6	39.9	1.4	1.5	5935	0.21	0.5	$5.8 \cdot 10^{-5}$	$1.7 \cdot 10^{-4}$	46
110625A	Swift	44.5	52.3	40	2.0	1.44	5892	-1.15	-1.38	$4.9 \cdot 10^{-4}$	$1.2 \cdot 10^{-3}$	3
110626A	Fermi	6.4	9.9	40.4	1.4	CPL	5892	0.19	0.41	-	$4.3 \cdot 10^{-4}$	-

Table 2—Continued

GRB	Satellite	Δt_{90}	$\Delta t'_{90}$	θ	\sqrt{F}	Spectral Index	A_{det}	σ	σ'	Fluence U.L. ^{a,c}	Fluence U.L. ^{b,c}	E_{cut} U.L. ^d
(1)	(2)	(s)	(s)	($^{\circ}$)	(6)	(α_{sat})	(m ²)	(9)	(10)	(erg cm ⁻²) (f_{sat})	(erg cm ⁻²) ($f_{2.5}$)	(GeV)
(1)	(2)	(3)	(4)	(5)	(6)	(7)	(8)	(9)	(10)	(11)	(12)	(13)
110629A	Fermi	61.7	70.6	5.1	1.9	CPL	6065	1.23	1.53	—	$2.8 \cdot 10^{-4}$	-
110705B	Fermi	19.2	29.2	18.8	1.6	CPL	5892	-1.09	-1.28	—	$9.5 \cdot 10^{-5}$	-
110709A	Swift	44.7	46.7	13.5	2.3	1.24	6021	0.48	0.34	$9.4 \cdot 10^{-5}$	$2.3 \cdot 10^{-4}$	< 2
110709C	Fermi	24.1	32.6	26.7	2	CPL	5935	-1.39	-1.21	—	$2.2 \cdot 10^{-4}$	-
110820A	Swift	256	256.0	41.6	4.7	1.92	5978	1.63	1.63	$9.6 \cdot 10^{-3}$	$1.6 \cdot 10^{-2}$	-
110915A	Swift	78.8	95.7	39.5	1.9	CPL	5848	1.01	0.65	—	$2.8 \cdot 10^{-3}$	-
110919A	Fermi	35.1	46.3	42.6	1.7	CPL	5848	0.04	0.33	—	$1.3 \cdot 10^{-3}$	-
110921A	Swift	48.0	55.6	7.2	2.1	1.57	5762	1.98	1.82	$1.6 \cdot 10^{-4}$	$3.3 \cdot 10^{-4}$	12
110928B	Fermi	148.2	161	8.5	2	1.92	5068	0.26	-0.03	$2.5 \cdot 10^{-4}$	$4.0 \cdot 10^{-4}$	-
111017A	Fermi	11.1	17.7	40	1.4	CPL	5892	-2	-1.16	—	$3.3 \cdot 10^{-4}$	-
111024C	Fermi	1.8	2.6	32.2	1.2	CPL	3812	-0.99	0.26	—	$3.7 \cdot 10^{-5}$	-
111103B	Swift	167	167.0	41.6	3.0	1.41	5892	1.6	1.60	$3.2 \cdot 10^{-3}$	$8.1 \cdot 10^{-3}$	14
111109C	Fermi	9.7	11.9	32	1.9	CPL	5848	0.79	0.8	—	$2.5 \cdot 10^{-4}$	-
111113A	IPN	0.5	-	28.4	1.4	CPL	5805	0.26	-	—	$3.8 \cdot 10^{-5}$	-
111208A	Swift	20	20.2	11.1	2.6	1.5	5112	-0.97	-0.97	$5.6 \cdot 10^{-5}$	$1.2 \cdot 10^{-4}$	6
111215A	Swift	796	796.0	30.6	23.5	1.7	5848	0.65	0.65	$2.0 \cdot 10^{-2}$	$4.0 \cdot 10^{-2}$	-
111228B	Fermi	2.9	4.2	23.9	1.4	CPL	5588	-1.26	0.13	—	$2.9 \cdot 10^{-5}$	-
120102A	Swift	38.7	38.7	44.8	2.4	1.59	5545	1.51	1.51	$1.3 \cdot 10^{-3}$	$2.8 \cdot 10^{-3}$	-
120106A	Swift	61.6	61.6	35.4	2.6	1.53	5588	-0.24	-0.24	$1.0 \cdot 10^{-3}$	$2.4 \cdot 10^{-3}$	-
120118B	Swift	23.3	23.3	42.7	2.5	2.08	5502	0.79	0.79	$1.3 \cdot 10^{-3}$	$1.9 \cdot 10^{-3}$	-
120118C	Fermi	17.2	17.2	18.1	2.3	CPL	5458	1.1	1.1	—	$2.5 \cdot 10^{-4}$	-
120129A	IPN	4	6.3	38.5	1.5	2.9	5718	-0.07	0.29	$5.0 \cdot 10^{-4}$	$3.5 \cdot 10^{-4}$	-

Table 2—Continued

GRB	Satellite	Δt_{90}	$\Delta t'_{90}$	θ	\sqrt{F}	Spectral Index	A_{det}	σ	σ'	Fluence U.L. ^{a,c}	Fluence U.L. ^{b,c}	E_{cut} U.L. ^d
(1)	(2)	(s)	(s)	($^{\circ}$)	(6)	(α_{sat})	(m^2)	(9)	(10)	($erg\ cm^{-2}$) (f_{sat})	($erg\ cm^{-2}$) ($f_{2.5}$)	(GeV)
(1)	(2)	(3)	(4)	(5)	(6)	(7)	(8)	(9)	(10)	(11)	(12)	(13)
120202A	Integral	100	104.1	15.6	4.0	-	5718	-0.14	-0.23	—	$7.6 \cdot 10^{-4}$	-
120217A	Fermi	5.9	8.4	38.8	1.5	CPL	5458	0.79	1.03	—	$5.3 \cdot 10^{-4}$	-
120219A	Swift	90.5	90.5	32	3.4	CPL	5545	-0.56	-0.56	—	$9.8 \cdot 10^{-4}$	-
120222A	Fermi	1.1	-	44	1.4	CPL	5588	0.43	-	—	$1.5 \cdot 10^{-4}$	-
120223A	Fermi	14.3	16	37.6	2	CPL	5632	0.39	0.49	—	$1.0 \cdot 10^{-3}$	-
120226B	Fermi	14.6	18.1	36.8	1.9	CPL	5632	-0.64	-0.77	—	$7.6 \cdot 10^{-4}$	-
120509A	Fermi	0.7	-	14.2	1.3	-	5892	-0.33	-	—	$1.3 \cdot 10^{-5}$	-
120512A	Integral	40	47.2	36.8	1.9	CPL	5892	0.06	-0.29	—	$1.5 \cdot 10^{-3}$	-
120519A	IPN	1.2	-	44.8	1.3	CPL	5935	-2.02	-	—	$6.9 \cdot 10^{-5}$	-
120522B	Fermi	28.2	38.9	40.2	1.6	<i>2.04</i>	5892	0.75	1.16	$8.4 \cdot 10^{-4}$	$1.3 \cdot 10^{-3}$	-
120604B	Fermi	12.0	16.9	33.5	1.6	1.73	5892	0.91	0.63	$1.2 \cdot 10^{-4}$	$2.4 \cdot 10^{-4}$	-
120612B	Fermi	63.2	71.4	21.5	1.8	1.57	4375	0.68	0.83	$2.0 \cdot 10^{-4}$	$4.0 \cdot 10^{-4}$	-
120625A	Fermi	7.4	11.1	21.2	1.5	<i>2.30</i>	5805	-0.27	-0.46	$5.8 \cdot 10^{-5}$	$6.8 \cdot 10^{-5}$	-
120630A	Swift	0.6	-	13.6	1.3	1.04	5632	-0.78	-	$3.5 \cdot 10^{-6}$	$1.1 \cdot 10^{-5}$	< 2
120703C	Fermi	77.6	77.6	21.8	2.5	1.68	5675	0.32	0.32	$2.6 \cdot 10^{-4}$	$4.9 \cdot 10^{-4}$	-
120727354	Fermi	0.90	-	5	1.3	-	5892	-1.25	-	—	$9.8 \cdot 10^{-6}$	-
120819A	Swift	71	71.0	42.1	2.8	1.49	5892	0.55	0.55	$1.5 \cdot 10^{-3}$	$3.6 \cdot 10^{-3}$	-
120905657	Fermi	195.6	235.2	41.8	4.4	-	5935	-2.03	-1.66	—	$4.9 \cdot 10^{-3}$	-
120915474	Fermi	5.9	8.3	40.9	1.5	-	5935	-0.08	-0.2	—	$4.2 \cdot 10^{-4}$	-
121011A	Swift	75.6	75.6	19.3	2.2	CPL	5805	-0.1	-0.10	—	$3.6 \cdot 10^{-4}$	-
121012A	Fermi	0.45	-	24.7	1.3	CPL	5805	0.7	-	—	$2.4 \cdot 10^{-5}$	-
121025A	MAXI/ISS	20	30.6	6.9	1.4	-	3596	0.52	0.38	—	$1.2 \cdot 10^{-4}$	-

Table 2—Continued

GRB	Satellite	Δt_{90}	$\Delta t'_{90}$	θ	\sqrt{F}	Spectral Index	A_{det}	σ	σ'	Fluence U.L. ^{a,c}	Fluence U.L. ^{b,c}	E_{cut} U.L. ^d
(1)	(2)	(s)	(s)	($^{\circ}$)	(6)	(α_{sat})	(m ²)	(9)	(10)	(erg cm ⁻²) (f_{sat})	(erg cm ⁻²) ($f_{2.5}$)	(GeV)
(1)	(2)	(3)	(4)	(5)	(6)	(7)	(8)	(9)	(10)	(11)	(12)	(13)
121108A	Swift	89	89.0	36.1	3.3	2.28	5718	-0.19	-0.19	$3.1 \cdot 10^{-3}$	$3.8 \cdot 10^{-3}$	-
121113544	Fermi	95.5	95.5	34.5	3.1	-	5718	0.6	0.6	—	$1.3 \cdot 10^{-3}$	-
121123A	Swift	317	317.0	42.1	4.9	CPL	5935	-0.25	-0.25	—	$1.2 \cdot 10^{-2}$	-
121202A	Swift	20.1	24.1	27.2	2.1	1.59	5632	0.67	0.84	$1.8 \cdot 10^{-4}$	$3.9 \cdot 10^{-4}$	34
130116415	Fermi	66.8	66.8	41.1	3.4	-	5718	-0.24	-0.24	—	$3.3 \cdot 10^{-3}$	-
130122A	Swift	64	64.0	30.6	2.4	1.34	5762	-0.23	-0.23	$2.3 \cdot 10^{-4}$	$6.0 \cdot 10^{-4}$	7

Note. —

^aUsing the spectrum determined by satellites.

^bAssuming a differential spectral index 2.5.

^c99% c.l.

^dDerived from the f_{sat} Fluence U.L. (see text).

Column 1 is the GRB name corresponding to the detection date in UT (YYMMDD). Column 2 gives the satellite that detected the burst. Column 3 gives the burst duration Δt_{90} as measured by the respective satellite. Column 4 gives the extended burst duration $\Delta t'_{90}$. Column 5 gives the zenith angle with respect to the detector location. Column 6 gives the square root of the Fano factor. Column 7 reports the spectral index: "CPL" means that the spectrum measured by the satellite is better fitted with a cutoff power law. In case of double power law fit (Band or SBPL functions) the higher energy spectral index is reported (in italics). Column 8 gives the detector active area for that burst. Columns 9 and 10 give the statistical significance of the on-source counts over the background for standard and extended burst duration. Columns 11 and 12 give the 99% confidence upper limits on the fluence between 1 and 100 GeV for spectral index of Column 7 and fixed value -2.5, respectively. Column 13 gives the cutoff upper limit, if any.